ABSTRACT

COMPUTATIONAL AND EXPERIMENTAL DETERMINATION OF THE HYDRODYNAMICS IN A STIRRED UNBAFFLED VESSEL PROVIDED WITH ANGLE-MOUNTED AXIAL IMPELLERS

by

Ji Ma

In most industrial applications, stirred tanks and reactors are typically provided with baffles to improve their mixing characteristics. However, in a number of pharmaceutical production facilities unbaffled vessels are commonly used. The absence of baffles is preferred in such cases because it reduces the potential for contamination and makes cleaning the vessel between batches easier. However, the lack of baffles also has a negative impact on the system's hydrodynamics since it often results in poor mixing of the batch, especially if the impeller is centrally placed, since the liquid in such a system is subject to a strong tangential flow, but low axial and radial flows. This hydrodynamic regime is highly undesirable if effective top-to-bottom liquid recirculation is required, and especially if a second phase (e.g., solid particles, immiscible liquids) must be dispersed and incorporated into the liquid bulk. For this reason, impellers in unbaffled pharmaceutical vessels are typically placed off-center, and, additionally, they may be mounted on a shaft that is angled with respect to the vessel vertical centerline. This lack of symmetry introduces some degree of "baffling" effects, in that it promotes stronger vertical recirculation of the liquid, and improves the suspension of settling solids and the incorporation of floating solids.

Despite their industrial relevance, especially for the pharmaceutical industry, extremely limited information is available on the hydrodynamics of vessels provided with angle-mounted impellers. Therefore, in this work, experimental and computational tools

were used to determine the hydrodynamics of fluids in a Plexiglas, custom-made, scaled-down version (diameter: 316 mm) of an industrial vessel with an elliptical bottom and provided with two angle-mounted (by 5° off the vertical) A-310 Lightnin impellers. The system was operated under different operating conditions in order to replicate the mixing characteristics of the industrial system. Computational Fluid Dynamics (CFD) was used to quantify the hydrodynamics of this system under different geometric configurations (such as liquid level), agitation speeds, and for different fluid rheologies. In all cases a multiple reference frame (MRF) computational approach was used and turbulence was modeled using the k-ε method. In addition, Particle Image Velocimetry (PIV) was used to experimentally determine the velocity flow field in water for some of these configurations in order to validate the CFD predictions, thus providing guidance on the optimal operation of these industrial system.

The results obtained here indicate that there is substantial agreement between the CFD predictions and the PIV experimental results. The flow in the vessel appears to be very complex. The axial pumping action of the impellers produces a downward flow impinging the bottom of the vessel resulting in flow splitting and in the formation of a less well-mixed zone near the vessel bottom that persists even when the impeller velocity is substantially increased. This zone could be the preferential location for the sedimentation of settling solids in the liquid.

COMPUTATIONAL AND EXPERIMENTAL DETERMINATION OF THE HYDRODYNAMICS IN A STIRRED UNBAFFLED VESSEL PROVIDED WITH ANGLE-MOUNTED AXIAL IMPELLERS

by
Ji Ma

A Thesis
Submitted to the Faculty of
New Jersey Institute of Technology
in Partial Fulfillment of the Requirements for the Degree of
Master of Science in Pharmaceutical Engineering

Otto H. York Department of Chemical, Biological and Pharmaceutical Engineering

January 2016

APPROVAL PAGE

COMPUTATIONAL AND EXPERIMENTAL DETERMINATION OF THE HYDRODYNAMICS IN A STIRRED UNBAFFLED VESSEL PROVIDED WITH ANGLE-MOUNTED AXIAL IMPELLERS

Ji Ma

Dr. Piero M. Armenante, Thesis Advisor — Date
Distinguished Professor of Chemical Engineering, NJIT
Director, Pharmaceutical Engineering Program, NJIT

Dr. Norman Loney, Committee Member — Date
Professor of Chemical Engineering, NJIT

Dr. Laurent Simon, Committee Member — Date
Associate Professor of Chemical Engineering, NJIT

BIOGRAPHICAL SKETCH

Author: Ji Ma

Degree: Master of Science

Date: January 2016

Undergraduate and Graduate Education:

- Master of Science in Pharmaceutical Engineering,
  New Jersey Institute of Technology, Newark, NJ, 2015

- Bachelor of Engineering in Pharmaceutical Engineering,
  Hebei University of Technology, Tianjin, P. R. China, 2011

Major: Pharmaceutical Engineering

To my beloved parents who are the rocks of my family, the source of my power, and the guidance of my life.

ACKNOWLEDGMENT

I would like to express my deepest gratitude to Dr. Piero Armenante, my advisor, for not only giving me the opportunity to work with him, but also for contributing his expertise and insights during the course of my research. I would also like to give my sincerest appreciation to NJIT for giving me the opportunity to start a new chapter of my life and making me something more than a student.

Furthermore, I would like to give a special thanks to Bing Wang who lent me her prior research experience in this field and support in my work. For the constant support and encouragement that was given to me by my family, especially my parents, that motivated me to not only finish my thesis and academic career, but also be a success in all of my endeavors: Thank you.

TABLE OF CONTENTS

TABLE OF CONTENTS
(Continued)

LIST OF TABLES

Table **Page**

LIST OF FIGURES

LIST OF FIGURES
(Continued)

Figure **Page**

LIST OF FIGURES
(Continued)

Figure **Page**

LIST OF SYMBOLS

N	Rotation speed of impeller
D_i	Diameter of impeller
μ	Fluid viscosity
μ_t	Eddy viscosity
μ_τ	Tangential velocity
Re	Reynolds number
k	Turbulence kinetic energy
ε	Dissipation rate
ω	Specific dissipation rate
α, β, σ	Closure coefficients
f_β	Round-jet function
χ_ω	Absolute value of Pope's nondimensional measure of vortex stretching parameter
$\boldsymbol{\Omega}_{ij}$	Rotation tensor
x_i	Position vector
$C_1, C_2, \sigma_\varepsilon, \sigma_k$	Empirical constants for k-ε Turbulence Model

CHAPTER 1

INTRODUCTION

Background and Overall Objective

Stirred tanks and reactors provided with baffles are commonly utilized in most industrial applications. Therefore, a significant literature exists on these systems, and a number of studies have examine not only their hydrodynamics but also additional phenomena such as blend time, solid suspension, power dissipation, and others. On the other hand, glass-lined, unbaffled reactors with angled-mounted impellers, i.e., impellers mounted on a shaft oriented at an angle with respect to the vessel centerline, are frequently used in the pharmaceutical industry to implement a variety of unit operations. A glass-lined reactor without baffles can provide a smooth surface for excellent cleanability, material compatibility, corrosion resistance, and lower instrument cost [1]. However, this type of reactors, if provided with only a centered impeller are associated with significant swirling, low axial velocities, inadequate dispersions of dispersed phases, such as fine solids and, in general, poor mixing of the reactor's content. The use of angle-mounted impellers can alleviate many of these problems, most importantly including the reduction or elimination of the swirling action, so that the mixing efficiency is better in these reactors. This is especially so if the shaft is not only angled, but also placed off center with respect to the vessel centerline. Possible issues associated with angled-mounted impeller systems are that these systems are more limited than vertical-shaft system because of mechanical issues, such as the weight of impeller and shaft, and the low center of gravity, resulting in a significant bending moment and the need for reduced agitation speeds.

Despite their industrial relevance, tanks and reactors provided with angle-mounted impellers have received very little attention in the literature. In particular, no information is available on the hydrodynamics of these systems. Myers et al. (2011) studied solid suspension in flat-bottom tank provided with a single off-center impeller. When an axial-flow impeller was used in this configuration, the suspension was achieved at agitation speed lower than in centrally mounted systems. Ram et al. (2000) examined mixing times in stirred vessels and obtained a correlation limited to the system that they studied. Myers et al. (2002) reviewed the effect of baffling in general on solid suspension and very briefly also examined angle-mounted impellers.

Therefore, the overall objective of the work describe here is to use experimental and computational tools to determination of the hydrodynamics of a model fluid in a scaled-down version of an industrial tank provided with angle-mounted impellers under different operating conditions in order to replicate the mixing characteristics of the industrial system. Similarly to the approach used in recent NJIT-Merck projects (Zhang et al., 2013, Wang el al. 2013), Computational Fluid Dynamics (CFD) was used here to quantify the hydrodynamics of this system under different geometric configurations, and agitation speeds. In addition, Particle Image Velocimetry (PIV) was used to experimentally determine the velocity flow field for some of these configurations in order to validate the CFD predictions, thus providing guidance on the optimal operation of the industrial system.

Specific Objectives and Approach

In this study, CFD was utilized to simulate the flow pattern in a scale down version of an actual full-scale, glass-lined reactor equipped with two three-blade A-310 Lightnin

fluidfoil impellers installed on a shaft that was vertically tilted by five degrees off the vessel centerline. The system under study was a custom-built Plexiglas tank 303.9-mm in diameter. The specific objectives of this work were to predict the system's hydrodynamics at three agitation speeds representing the conditions that would be used for scale-up/scale down of an actual industrial system using different criteria. The laboratory system was studies at 60 rpm since this is the operating agitation speed in the actual full-scale system. Using this speed also for the laboratory scale reactor would imply studying the hydrodynamics at constant mixing (blend) time, since keeping the agitation speed constant is equivalent to maintaining constant mixing time across scales. This was taken as the basic case. In addition, CFD simulation were conducted using different turbulence models, i.e., the standard *k*-ε model, a low Reynolds number *k*-ε model called Abid model and the standard k-ω model.

If the power dissipation per unit volume is kept constant upon scale up this is equivalent to keeping the term N^2D^3=constant for geometrically similar systems, where N is the impeller agitation speed and D is the impeller diameter. In the specific case, this was equivalent to studying the laboratory system at an agitation speed equal to 182 rpm. Finally, the system was studied at N=317 rpm, which is equivalent to maintaining the impeller tip speed velocity identical across scales (ND=constant).

In order to ensure that the CFD results are meaningful, the CFD predictions needed to be compared to experimental data. Therefore, an additional specific objective of this work was used PIV to obtain experimentally velocity measurement that could be used to validate the CFD results.

CHAPTER 2

EXPERIMENTAL SYSTEM AND PARTICLE IMAGE VELOCITY (PIV)

2.1 Mixing System Apparatus

The mixing system studied in this work consisted of a scaled down version of an actual large-scale industrial mixing system used in the pharmaceutical industry. The vessel used here was a custom-designed, cylindrical, Plexiglas tank (manufactured by Indelco, Inc., Memphis, TN) with an internal diameter of 303.9 mm, an overall height of 630 mm, and an elliptical bottom having its major axis equal to the tank diameter and its minor axis radius equal to 111.5 mm, as shown in Figure 2.1. This vessel was placed in, and fixed to, a square tank filled with water. This installation was used to minimize refractive effects at the curved surface of the vessel wall when the light went through different medium with different refractive index (Figure 2.3). The cylindrical tank was filled with distilled water up to a liquid level of 550mm (Figure 2.1).

The agitation system consisted of two downpumping A-310 Lightnin impellers (curtesy of Richard Kehn of SPX Flow Technology, Rochester, NY) with a diameter of 86.3 mm mounted in the middle and at the lower end of a stainless steel shaft 12.6mm in diameter and 610 in length. The distance between the impellers was 170.2 mm (center-to-center). The impellers were assembled on the shaft so that their blades were vertically aligned (Figure 2.2).

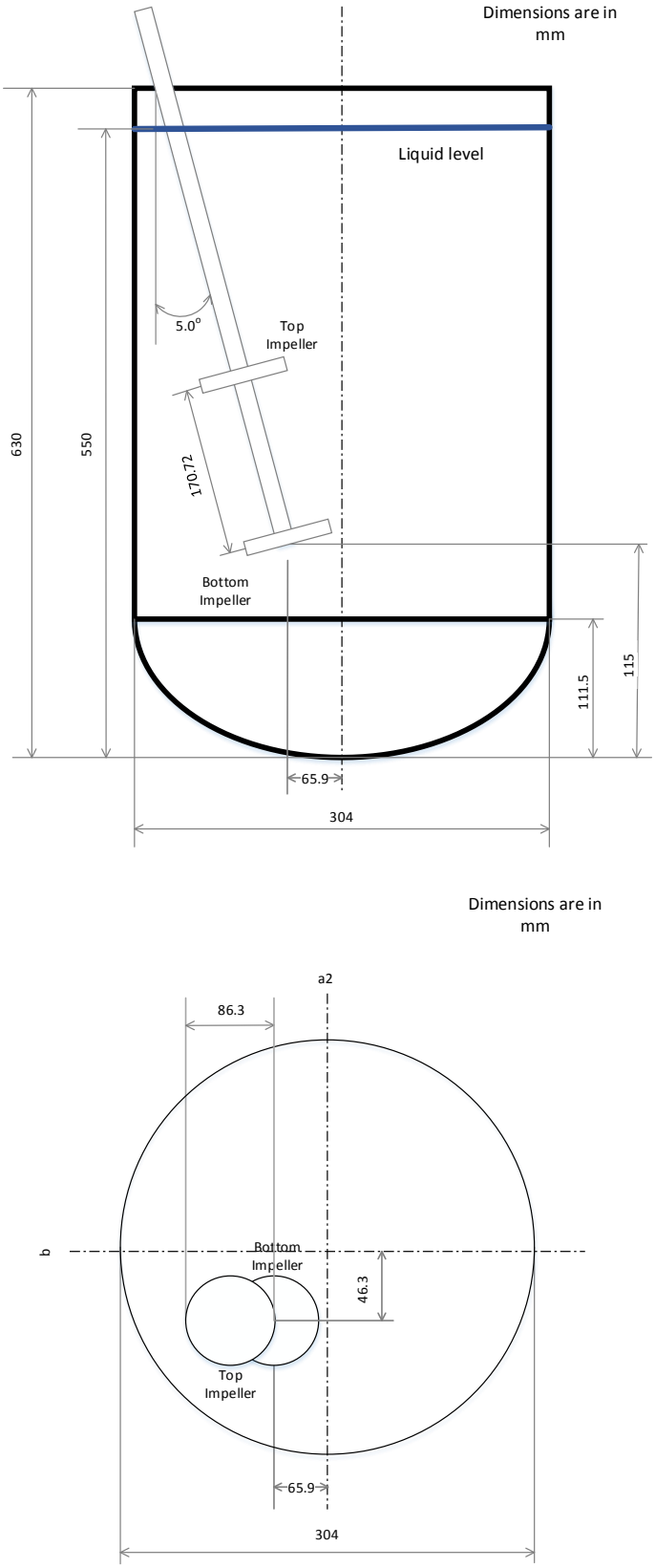

Figure 2.1 Mixing system: side view (top panel) and top view (bottom panel).

Figure 2.2 Shaft and impellers.

Figure 2.3 Agitation system.

As what the pictures show above, the shaft was connected to a motor (Model CG-2033-11; Chemglass Life Sciences, Vineland, NJ) (Figure 2.4) whose rotation speed could be controlled by an external controller. The agitation speed could be adjusted in the range 0-500 rpm within ±1 rpm (Figure 2.5). The vessel, square tank, motor, and impellers were placed on a metal rack assembled with steel plates and rods so that the position of the agitation system (motor, shaft, and impellers) with respect to the vessel could be adjusted as desired (Figure 2.3). The impeller-shaft assembly was mounted on an off-centered angled position which was five degrees off the vertical and lying, when seen from above, on a vertical plane 46.3 mm to the right of the plane b which passes through vessel centerline and parallel to the impeller shaft. The shaft was positioned so that its lower end was 115 mm from the vessel bottom and 65.9 mm from the plane a2 which perpendicular to the plane b and passing through the vessel centerline (Figure 2.1). The vessel, motor and impellers were placed on a steel falsework on which steel rods were fixed as a shelf to keep angled shaft stable (Figure 2.6).

Figure 2.4 Chemglass motor.

Figure 2.5 Chemglass external motor controller.

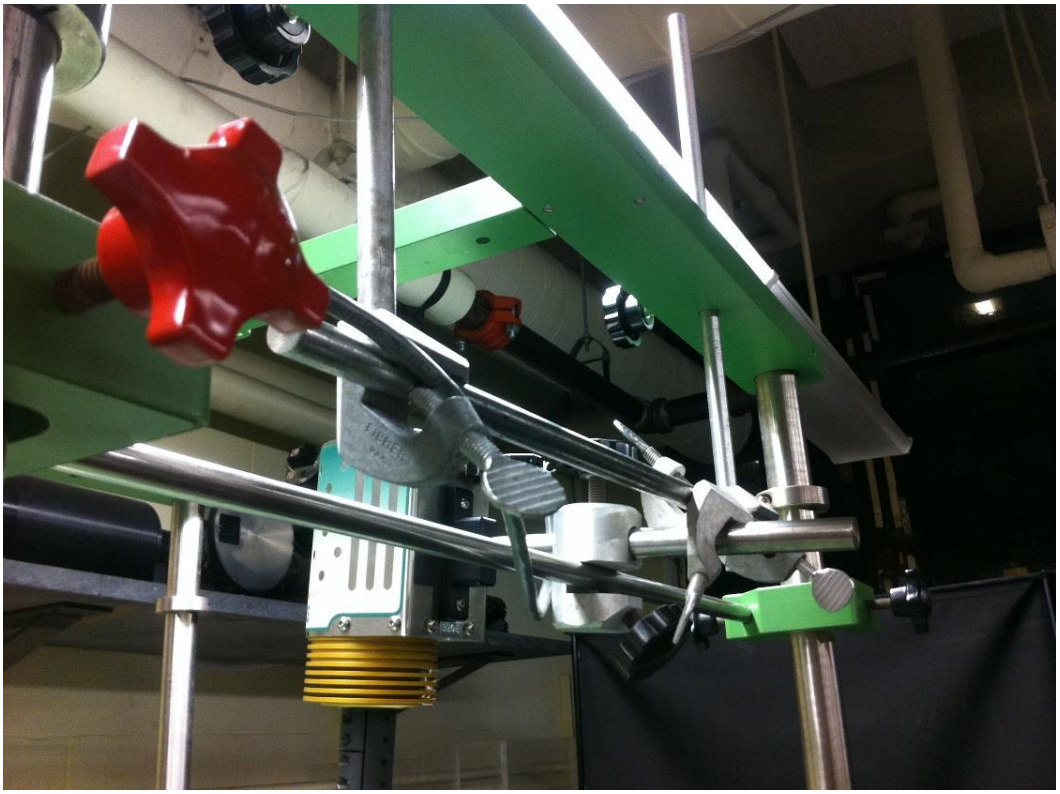

Figure 2.6 Details of mounting rack with motor.

In order to make sure that the angled shaft and impellers were installed at the right position, the bottom plane of square box was taken as the datum plane, and the connection points of the dotted line and the inner edge of the vessel in Figure 2.1 (bottom) were taken

as datum points. Before adjust the position of the vessel to make the edges of square box parallel to edges of the rack, a leveling gauge was used to ensure that base plate on which the vessel and tank rested was even. According to the Figure 2.1, the liquid level and the positions where the shaft initially contact the solution on the top and the ending point of the shaft were illustrated, the two points can be easily projected on the wall of square box and were marked. So that the motor and the shelf consisted with steel rods were adjusted to meet the requirements. The final step of agitation system adjusting was using the leveling instrument to test if the vessel was even.

2.2 PIV Apparatus

A Dantec FlowMap 1500 2D Particle Image Velocimetry (PIV) apparatus (Dantec Dynamics A/S, Tonsbakken 16 – 18, DK – 2740 Skovlunde, Denmark) was used to gather two dimensional information of the velocity field and flow pattern on a selected plane inside the system. The setup of the PIV apparatus is shown in Figure 2.7.

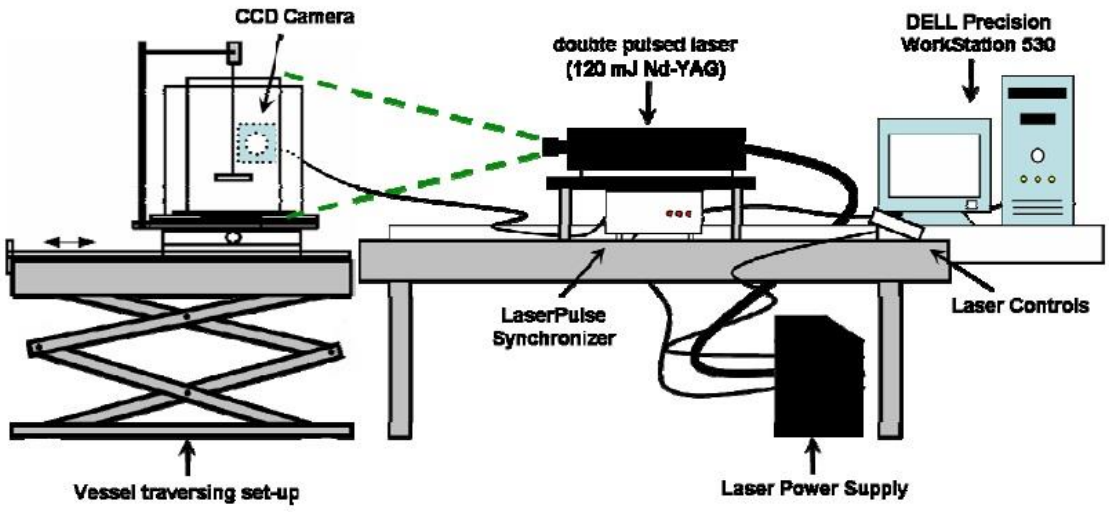

Figure 2.7 Schematic of laboratory PIV experimental set-up.

The PIV system consisted of a double pulsed 120 mJ Nd-Yag laser light source (New Wave Research model Solo 120 15 HZ, Fremont, CA, USA), a digital camera (Dantec Dynamics HiSense PIV/PLIF camera model C4742-53-12NRB, a synchronizer (LASERPULSE Synchronizer, TSI model 610034), and a computer (DELL Precision WorkStation 530) for data acquisition and data analysis. The laser source used in this study is classified into Class IV laser (a laser device can emit 532 nm wavelengths light). This emitter generates two pulsed infrared laser beam to form a laser light sheet by going through an optical arrangement of lenses and the light sheet passed through the solution seeded the tracer particles. Those tracer particles are silver-coated hollow borosilicate glass spheres (Dantec Measurement Technology USA, Mahwah, NJ, USA) with density of 1.4 g/cm^3 and size range from 2 to 20 μm (mean particle size 10 μm). When we use tracer particles to follow the fluid flow then calculate the fluid velocity, the gap time between two pulses is an important influence factor. For a certain situation, the higher velocity particles have, the shorter gap time should be. The laser light scattered by these particles was captured by a digital camera (Dantec Dynamics HiSense PIV/PLIF camera model C4742-53-12NRB), which was connected perpendicularly to the laser light sheet. A synchronizer (LASERPULSE Synchronizer, TSI model 610034) was connected to both laser and cameras to control the PIV measurement processes and the raw data analysis. The software which utilized to control PIV hardware and data analyze is called FlowManager Software. Each pair of images were sent to the work station will be divided into small sections called interrogation areas, then those areas was analyzed separately by using adaptive cross-correlation to calculate the speed of each particles which was divided into spatial x- and y-displacement. In this way, the vector that maximized the cross-correlation

function for that interrogation area. The resulting displacement vector obtained by dividing the x- and y- displacements was taken as the fluid velocity in that interrogation area during the gap time.

2.3 Materials and Method

In this study, the focus of the experimental work was to determine the flow pattern in the most critical section of the vessel, i.e., the bottom section. Since the system is non-symmetrical, which is very different from the ordinary vertically mounted impeller system, the velocity field was observed only in the lower portion of the vessel. In order to study the flow, two planes were chosen: vertical Plane a2 in the middle of the vessel, and Plane a1, parallel to Plane a2 but farther away from the impellers, i.e., closer to the camera (Figure 2.8 b) and 92.5 mm from the centerline. Each plane was divided into three sections when the PIV experiment were conducted because of the restriction of camera's field of view (Figure 2.8 a). In order to generate single images of the PIV velocity on any given cross section, the images representing the experimental PIV results in these sub-regions needed to be "stitched" together. These images were originally generated by FlowManager Software. A simple program written with Microsoft Windows Visual Studio 2008 was then utilized to assemble together the data of the three sub-regions. The lines drawn on the surface of square tank served as guides to determine the exact area that each image covered. The images slightly overlapped. The overlapping data were removed and a new complete data picture was created with the Tecplot 360 software.

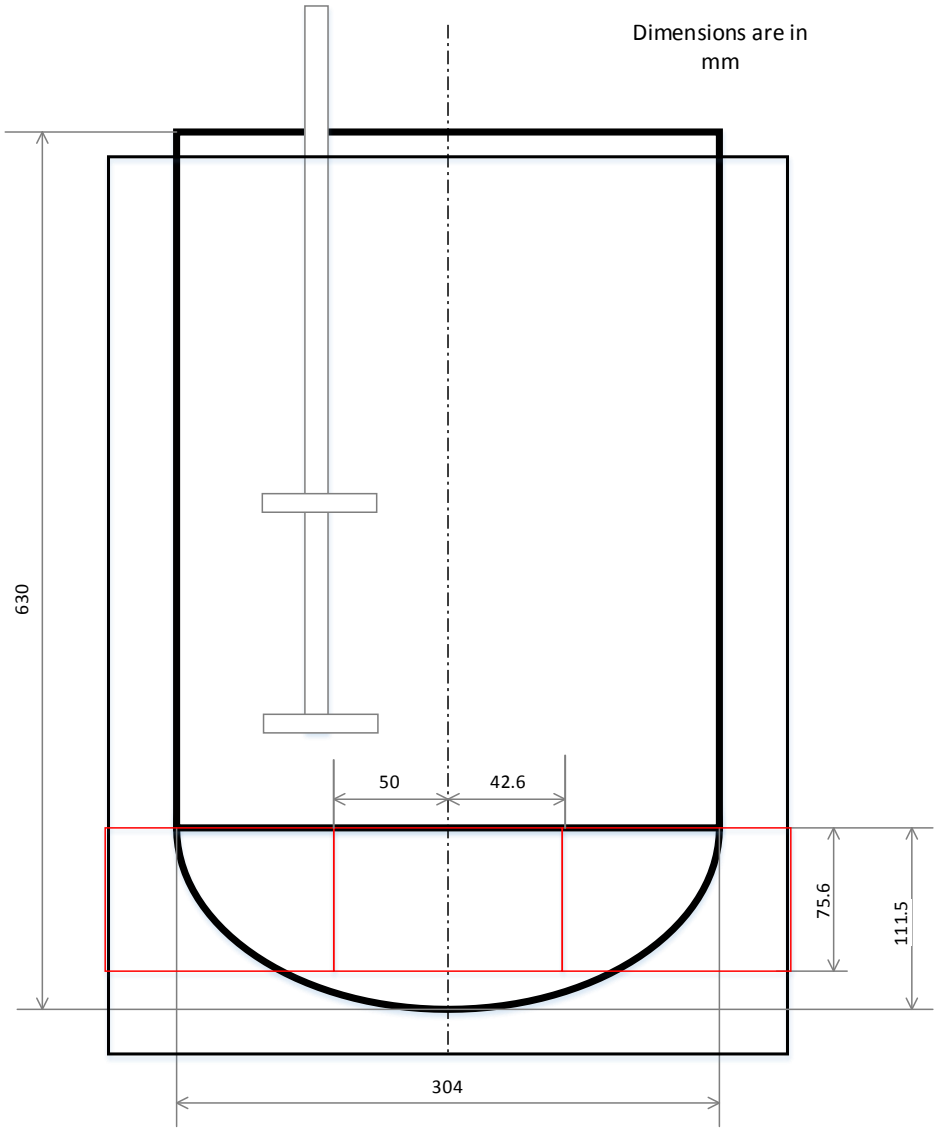

Figure 2.8 a Vessel and square box, front view.

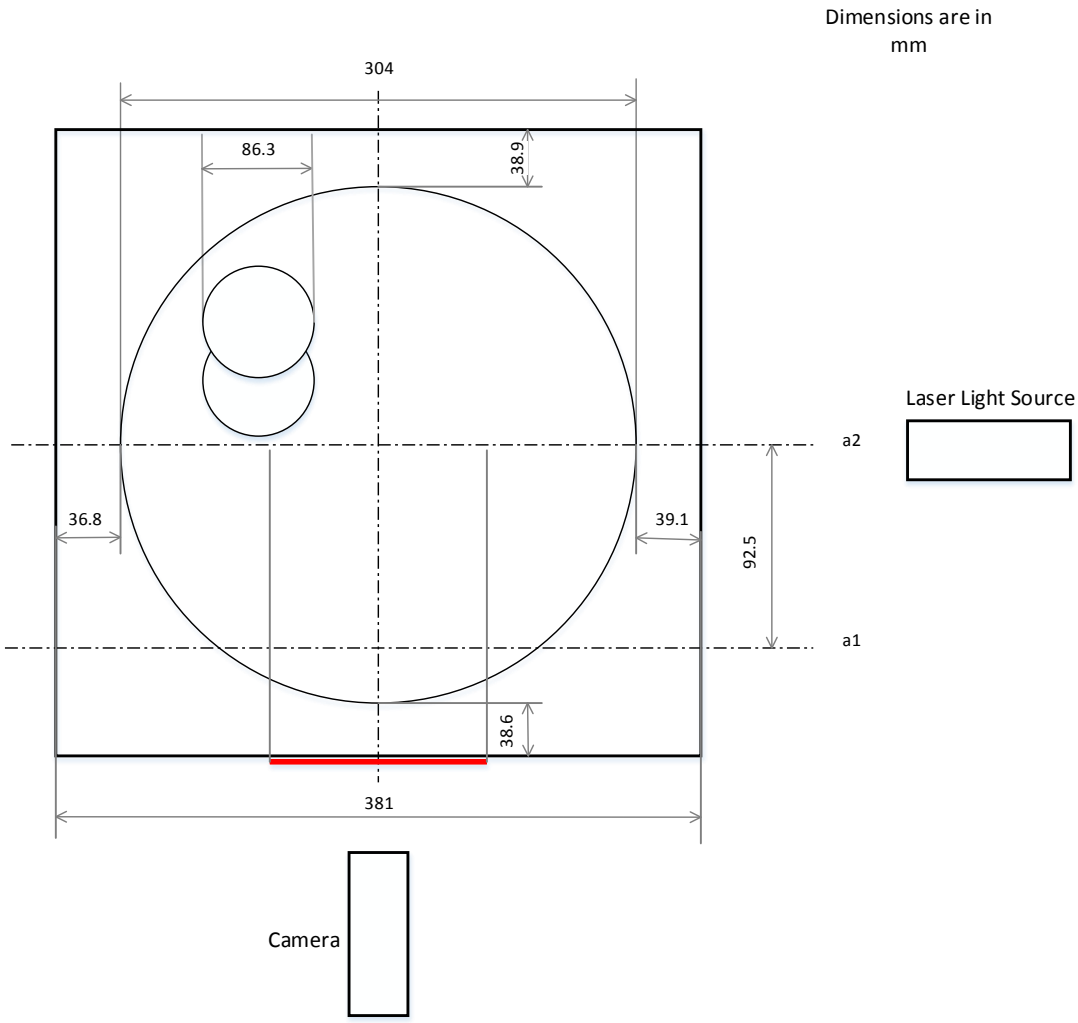

Figure 2.8 b Vessel and square box, top view.

Because the observed planes were divided into three sections, the boundaries were drew on the wall of square box to identify the position of camera (Figure 2.9)

Figure 2.9 Details of the elliptical tank bottom.

In the PIV experiment, one pair of images of the chosen section were taken once the laser pulse was activated, which were repeated 100 time in one process. Inevitably, the images may contain outside regions, therefore, image masks were defined and applied to all images to reject interference of outside parts. After the correction is applied to each image, the vector field of velocity is calculated and the statistical average of 100 pairs of images was finally formed. For further investigation, the profile should go through moving-range validation and average filter to obtain the final velocity vector map.

CHAPTER 3

COMPUTATIONAL APPROACH TO FLOW SIMULATION IN THE MIXING VESSEL

3.1 Simulation Method of Computational Fluid Dynamics (CFD)

3.1.1 Background and Theory

Computational Fluid Dynamics (CFD) is a branch of fluid mechanics that uses mathematical equations, numerical analysis and algorithms to study cases such as fluid flow, stressed component, heat transfer by discretizing and solving partial differential equations (PDEs) into solvable systems of equations. Partial derivatives created by the PDEs can be substituted with limited different quotients, which can be utilized into the inverse iteration with formulate difference equations. Those equations algebraically represent the PDE and are solvable. In CFD, the research object, or so called the studied system is decomposed into numbers of cells, which are arranged throughout the geometry of the subject and are basically classified as the mesh or the grid [1].

One of the earliest CFD calculations using finite differences and divided the geometry space into cells and grid was developed from the pioneering accomplishments of creative men such as Richardson (1910) and Courant, Friedrichs, and Lewy [3]. With the advance in computer science, the CFD, as a rapid rising science, attracted even more attention. Since the end of the 1960s, more and more scientists and technicians devoted in study of CFD which applied to quantities of industry fields, such as aerospace, oceanic flows, combustion, mechanical, mixing process, etc. [4].

CFD simulation has many more advantages than experimental method [5]. One of the most important advantages of CFD method is the saving of cost, including time, human labor, and space room. It is particularly valuable if the experiment can't be applied because of limitations, such as measurements the variable values of fluid in the sealed pipe. Another one is the research and development of new equipment or process.

In the last decade, CFD has been wildly used as a common tool to evaluate the performance of general equipment and operation units in industry, such as stirred mixing tanks [6], Packed-bed reactors [7], heat exchangers [8], and etc. CFD has become an essential part of process management, product design and equipment alteration in many companies of many areas because it can provide a trustworthy prediction in processes like hydrodynamics, heat transfer, mass transfer, chemical reaction, mechanical movement, and so on. It is easier compare the results of CFD and obtained experimental results of the optimized conditions or improved equipment which has been modified, enlarged, or improved product quality [9].

The CFD simulation can be performed by using different CFD software such as Ansys and Comsol in computer. There are three major tasks in the simulation process, pre-processing, processing and solving, and post-processing. In the first stage, pre-processing, the problem should be focused on is conceptualization and analysis of the physics of the system. Then structure geometry can be set up, mesh can be drew, and boundary conditions can be defined. In the processing and solving stage, the simulation shall begin. By using the relevant discretized conservation equation, each of the thousands of cells in which the control volume is divided will be iteratively calculated. The calculation process can be stopped when an acceptable convergence is achieved. In the

post-processing step, the case should be done, and the results can be obtained to do the following analysis and comparison. A solved case can provide information of field like temperature, concentration, pressure, velocity with 2D or 3D images of the vector and contour plots.

In this study, Fluent 6.3.26 and was used to simulate the 3D hydrodynamics of the stirred unbaffled vessel with angle-mounted axial impellers, and Gambit 2.4.6 is the software in which the geometry model was constructed. This simulation can predict the flow field, thus we can compare the CFD predictions with the PIV measurements.

3.1.2 Navier-Stokes and Turbulence Modeling

Conservation of energy, conservation of mass, and Newton's second law are three elementary principles we use to describe fluid in a control volume [2]. I assume that there the exchange of heat between the control volume and environment and the temperature effect on fluid can be ignored, then the energy equation won't be considered. For the turbulence fluid, conservation of mass and conservation of momentum can be written in Cartesian form as:

$$\frac{\partial u_1}{\partial x} + \frac{\partial u_2}{\partial y} + \frac{\partial u_3}{\partial z} = 0 \tag{3.1}$$

$$\frac{\partial u_i}{\partial \mathrm{t}} + \frac{\partial u_i u_j}{\partial x_j} = -\frac{1}{\rho}\frac{\partial P}{\partial x_i} + \nu\nabla^2 u_i + g_i \tag{3.2}$$

In turbulence flow, the fluid is much more complex than laminar flow, so there is an assumption that the velocity of any point is made of two parts: the sum of the mean (time-averaged) and fluctuating components, which is:

$$u_i = \bar{u}_i + u_i' \tag{3.3}$$

Then we have the equation of conservation of momentum of turbulence flow, as known as the Reynolds-averaged Navier-Stokes (RANS) equations. For the incompressible fluid:

$$\frac{\partial \bar{u}_i}{\partial t} + \bar{u}_j \frac{\partial \bar{u}_i}{\partial x_j} = -\frac{1}{\rho}\frac{\partial \bar{P}}{\partial x_i} + \nu \nabla^2 \bar{u}_i + g_i - \frac{\partial}{\partial x_j}\left(\overline{u_i' u_j'}\right) \tag{3.4}$$

where the terms on the left are the pressure forces, viscous transport, body forces, and Reynolds stresses.

Since the last term contains the velocity of fluctuating components, they are typically connected their relationships with other variables. One of the most acceptable assumption is "Boussinesq hypothesis", which includes two transportation equations.

$$\rho\overline{\mathrm{u'}_i \mathrm{u'}_j} = \frac{2}{3}\rho k \delta_{ij} + \left[\mu_t \left(\frac{\partial \bar{u}_i}{\partial x_j} + \frac{\partial \bar{u}_j}{\partial x_i}\right)\right] \tag{3.5}$$

$$\mu_t = \rho \mathrm{C}_\mu \frac{k^2}{\varepsilon} \tag{3.6}$$

Before the discussion of turbulence models, there is a fact we have to understand that no single turbulence model is all-powerful to solve all kinds of problems, they all have limitations. The choice of model depends on the property of flow, which means we have to know whether the flow can be classified as laminar or turbulence. To a mixing vessel, the judgement of flow can be made according to the expression of dimensionless Reynold number [10]:

$$Re = \frac{N_i {D_i}^2 \rho}{\mu} \tag{3.7}$$

where N is the impeller speed, D_i is the impeller diameter, and μ is the fluid viscosity.

The conversion interval of the flow from laminar to turbulence is Re= (50, 5000). To fully baffled system, full turbulent flow emerge when Re > 10^4, while the value should be Re > 10^5 to an unbaffled system [10]. Since the simulation of vessel with angled axial has never been studied before, two kind of turbulence models were utilized in this research. The introduction are presented below.

3.1.3 *k*-ε Turbulence Model

The series of *k*-ε model are semi-empirical models which contains two extra transportation equations for the turbulence kinetic energy k and its dissipation rate ε. In the standard *k*-ε model, an assumption that the flow is fully turbulent is made, which means viscous fluid or low Reynolds number fluid cannot be modified by *k*-ε model. Therefore, the standard *k*-ε model can only be applied to fully turbulent low-viscosity flow. The greatest advantage of standard *k*-ε model is it is so fully studied that this model can reliably explain complex turbulent flow, and the main disadvantage is the assumption that fluctuating velocities are isotropic. The governing transport equations for the standard k-ε model are:

$$\frac{\partial(\rho k)}{\partial t} + \frac{\partial}{\partial x_i}(\rho \bar{u}_i \mathrm{k}) = \frac{\partial}{\partial x_i}\left[\left(\mu + \frac{\mu_t}{\sigma_k}\right)\frac{\partial k}{\partial x_i}\right] + \mathrm{G}_k - \rho\epsilon \tag{3.8}$$

$$\frac{\partial(\rho \varepsilon)}{\partial t} + \frac{\partial}{\partial x_i}(\rho \bar{u}_i \varepsilon) = \frac{\partial}{\partial x_i}\left[\left(\mu + \frac{\mu_t}{\sigma_\varepsilon}\right)\frac{\partial \varepsilon}{\partial x_i}\right] + \mathrm{C}_1\frac{\varepsilon}{k}\mathrm{G}_k + \mathrm{C}_2\rho\frac{\varepsilon^2}{k} \tag{3.9}$$

where G_k is:

$$\mathrm{G}_k = \mu_t\left(\frac{\partial \bar{u}_i}{\partial x_i} + \frac{\partial \bar{u}_j}{\partial x_i}\right)\frac{\partial \bar{u}_i}{\partial x_j} \tag{3.10}$$

where μ is the dynamic fluid viscosity, μ_t is the eddy viscosity, G_k is the term for turbulence generation [11], C_1, C_2, σ_ε, and σ_k are empirical constants.

In order to apply k-ε model to low Reynolds flow, Abid model was invented in 1991 and some modifications were made to the equations above. Equation 2.9 was modified as follow:

$$\frac{\partial(\rho\varepsilon)}{\partial t} + \frac{\partial}{\partial x_i}(\rho\bar{u}_i\varepsilon) = \frac{\partial}{\partial x_i}\left[\left(\mu + \frac{\mu_t}{\sigma_\varepsilon}\right)\frac{\partial\varepsilon}{\partial x_i}\right] + C_1 f_1 \frac{\varepsilon}{k} G_k + C_2 f_2 \rho \frac{\varepsilon^2}{k} + E \qquad (3.11)$$

where ϵ, in the last term of equation 2.8, is $\varepsilon_0+\varepsilon$, then μ_t becomes:

$$\mu_t = \rho C_\mu f_\mu \frac{k^2}{\varepsilon} \qquad (3.12)$$

where $f_\mu = (1 + 3.4\sqrt{Re_t})\tanh(y^+/80)$, f_1 and f_2 are 1, $\varepsilon_0 = 2\mu(\partial\sqrt{k}/\partial y)^2$, E = 0, $Re_t = k^2/\varepsilon\mu$, $y^+ = u_\tau y/\mu$, the quantity u_τ is the mean tangential velocity, the quantity y is the distance from the wall [12]. The rest of the equations and constants are same to standard *k*-ε model.

3.1.4 Standard k-ω Turbulence Model

Similar to the standard *k*-ε model, the standard k-ω model is also an empirical model which based on model transport equations for the turbulence kinetic energy k and the specific dissipation rate ω, which is the ratio of k and μ_t. The standard k-ω model is an improvement of Wilcox k-ω model so that it can make an accurate prediction of free shear and low Reynolds number flows [12]. Plus, it has lower sensitivity to boundary conditions which means the low Reynolds number boundary condition will be appositely applied in fine meshes area. The two governing equations for the standard k-ω model are:

$$\frac{\partial \mathrm{k}}{\partial t} + U_j \frac{\partial \mathrm{k}}{\partial x_i} = \tau_{ij} \frac{\partial U_i}{\partial x_j} - \beta^* k\omega + \frac{\partial}{\partial x_i}\left[(\mu + \sigma^* \mu_t)\frac{\partial k}{\partial x_j}\right] \tag{3.13}$$

$$\frac{\partial \omega}{\partial t} + U_j \frac{\partial \omega}{\partial x_i} = \alpha \frac{\omega}{k} \tau_{ij} \frac{\partial U_i}{\partial x_j} - \beta\omega^2 + \frac{\partial}{\partial x_i}\left[(\mu + \sigma \mu_t)\frac{\partial \omega}{\partial x_j}\right] \tag{3.14}$$

where the last term of first equation and second equation represent the generation of turbulence kinetic energy due to mean velocity gradients, and the generation of ω. The closure coefficient appearing in standard k-ε model and auxiliary relations are [12] [13]:

$$\alpha=13/25, \quad \beta_0^*=9/100, \quad \beta_0=0.0708, \quad \sigma=1/2, \quad \sigma^*=3/5 \tag{3.15}$$

$$\beta = \beta_0 f_\beta, \qquad \beta^* = \beta_0^* f_{\beta^*}, \qquad f_\beta = \frac{1+85\chi_\omega}{1+100\chi_\omega} \tag{3.16}$$

$$\chi_\omega = \left|\frac{\Omega_{ij}\Omega_{jk}S_{ki}}{(\beta_0^*\omega)^3}\right|, \quad f_{\beta^*} = \begin{cases} 1, & \chi_k \le 0 \\ \frac{1+680\chi_k^2}{1+80\chi_k^2}, & \chi_k > 0 \end{cases}, \quad \chi_k \equiv \frac{1}{\omega^3}\frac{\partial k}{\partial x_j}\frac{\partial \omega}{\partial x_j} \tag{3.17}$$

where α, β, and σ are closure coefficients in the specific dissipation-rate equation. f_β is the round-jet function, χ_ω is the absolute value of Pope's non-dimensional measure of vortex stretching parameter, Ω_{ij} is the rotation tensor, and x_i is the position vector.

As a model which was designed for low Reynolds number situation, standard *k*-ε model can make a good prediction on flat fluidics, spherical fluidics, shear flow and compressible fluid. Good convergence cannot be easily achieved by using standard k-ω

turbulence model. Under relaxation parameters should to be carefully adjusted to let the simulation results well converged.

3.2 Definition of the Agitation System for CFD Simulations

The impellers used in the experiments and in the CFD simulations system were A-310 Lightnin impellers mentioned above. The actual impellers were carefully measured with a caliper and a digital angle finder ruler. Measurements were taken using a system of coordinates where a reference point, a line, and a plane were selected. Accordingly, the center point of the bottom side of impeller was taken as the origin of coordinate of 3D Cartesian coordinate system. Then one blade was chosen and the coordinates of four ending points were recorded. According to observations, the surface of the blades were casted with equal radii. Therefore, measurements were taken on the section of two tips and the middle of the blade to simulate the real one (Figure 3.1a and b). After the coordinates of pivotal points were found an additional test was conducted to ensure the accuracy of measurement. The angles of blade from the hub to the tip were measured, so did the angle of deviation which the edge of the blade diverge from the datum line (rectangular axle). Based on the measurements, a computational model of the impellers was set up and utilized in CFD simulations.

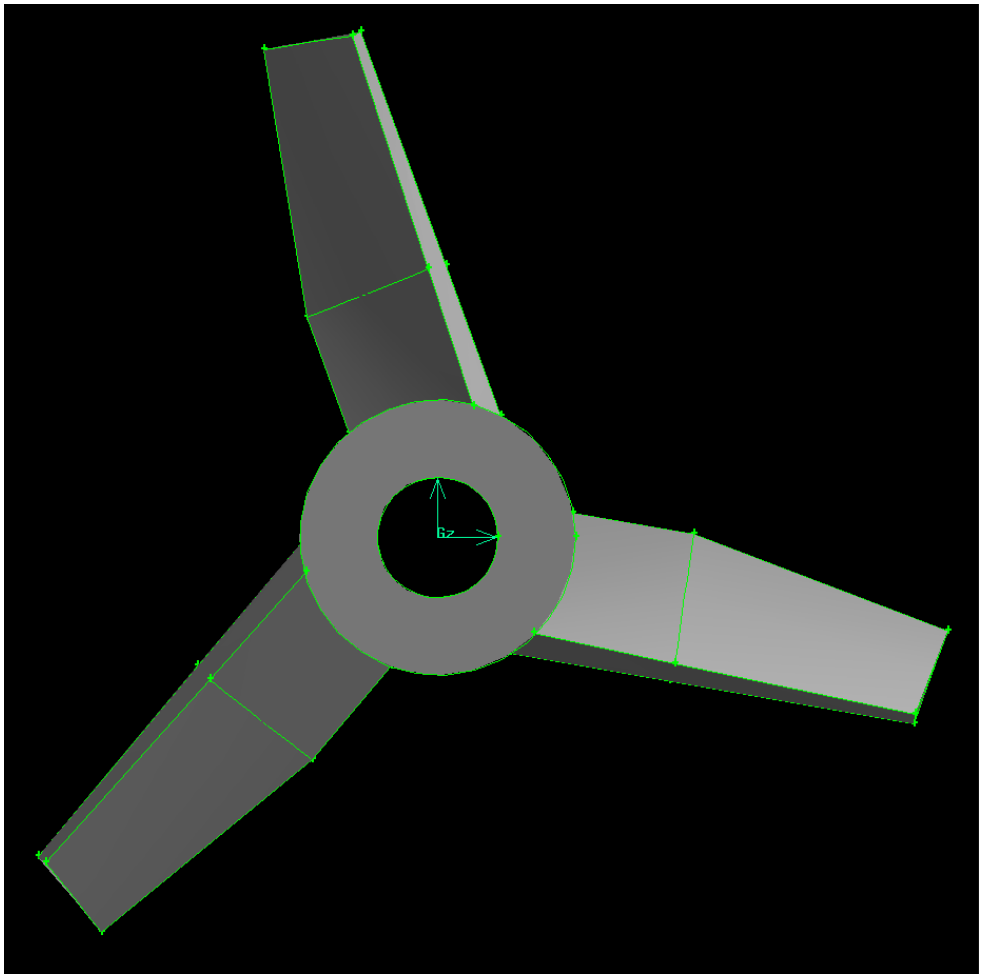

Figure 3.1 a Three-blade impeller geometry (top view).

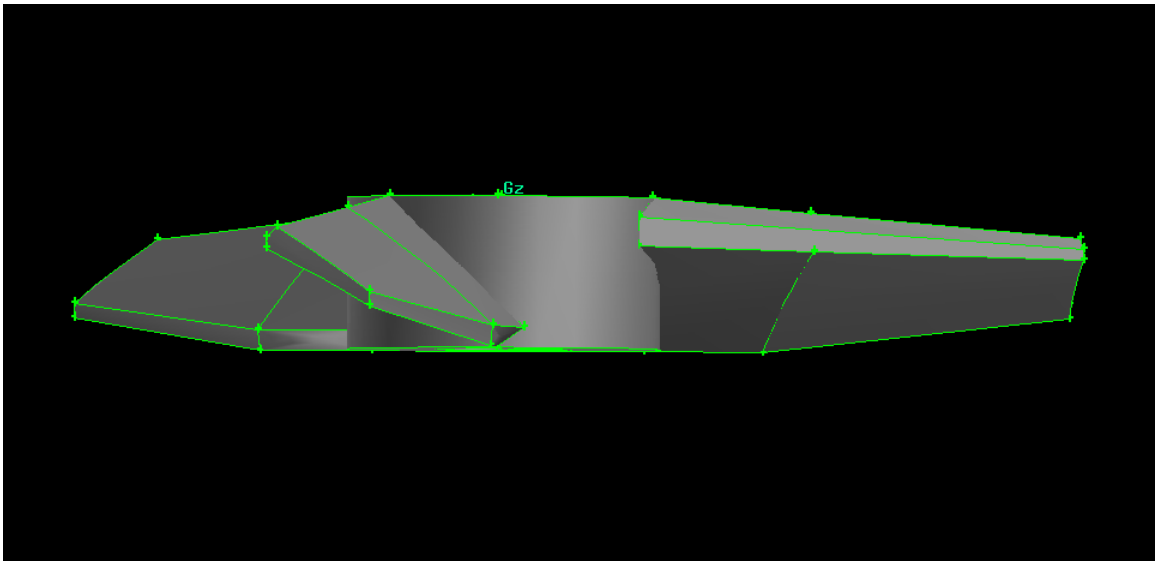

Figure 3.1 b Three-blade impeller geometry (side view).

3.3 Computational Mesh Used in CFD Simulations

The geometry of the system was built using the Gambit software (Figure 3.2). The computational mesh was generated to define the computational cells. Since the system is asymmetric, the whole system was divided into three domains and an unstructured tetrahedral mesh was utilized, as shown in Figure 3.3a, b, c, and d. The mesh developed for this system contained 1,466,794 cells and 267,872 nodes. To ensure a high quality mesh throughout the system, the average EquiSize Skew parameter was determined and was found to be 0.3 to 0.4. Similarly, the maximum skewness was 0.77.

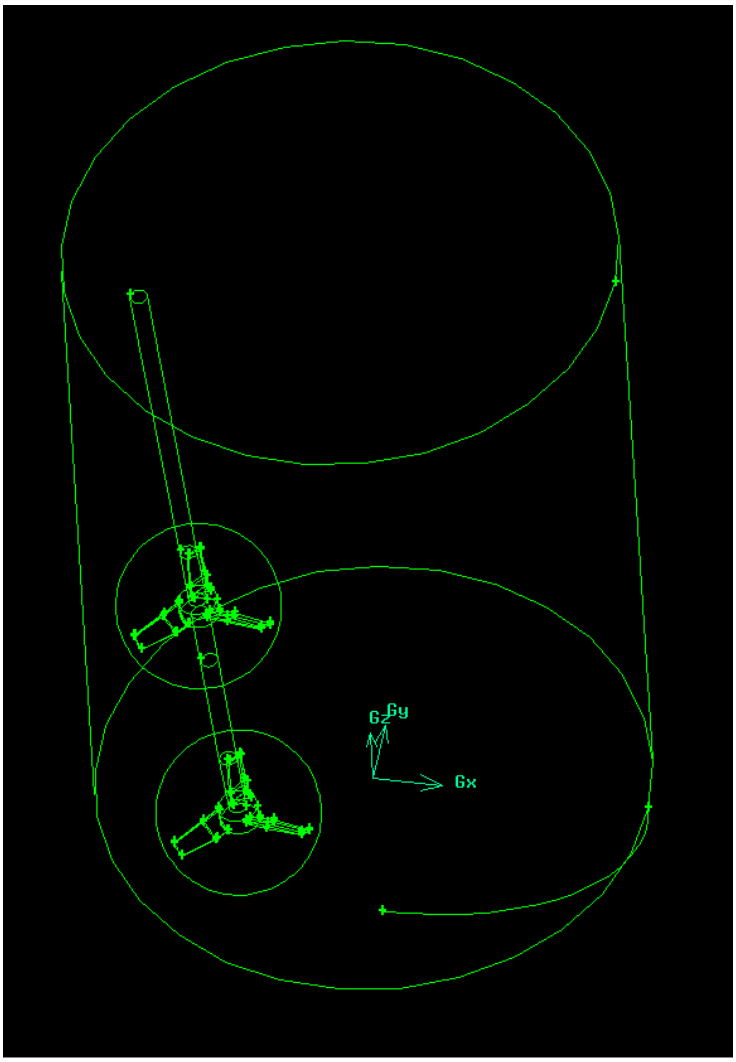

Figure 3.2 Geometry of the whole system, angular view.

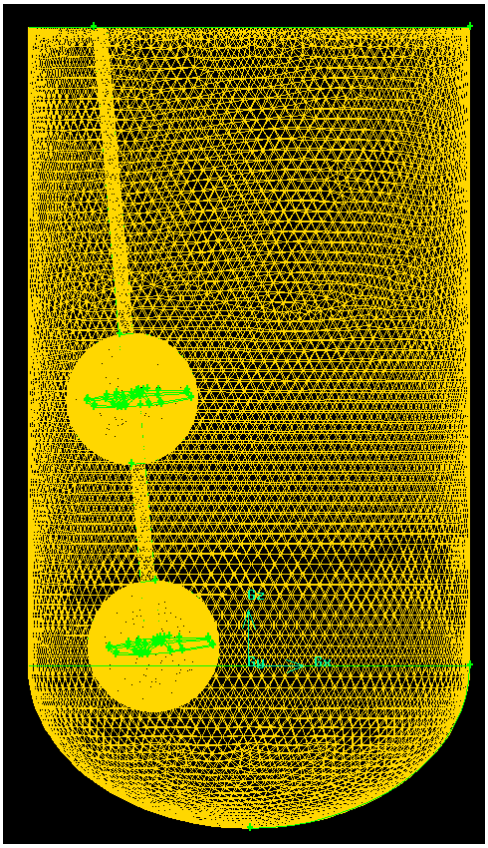

Figure 3.3a Meshing of whole system, side view.

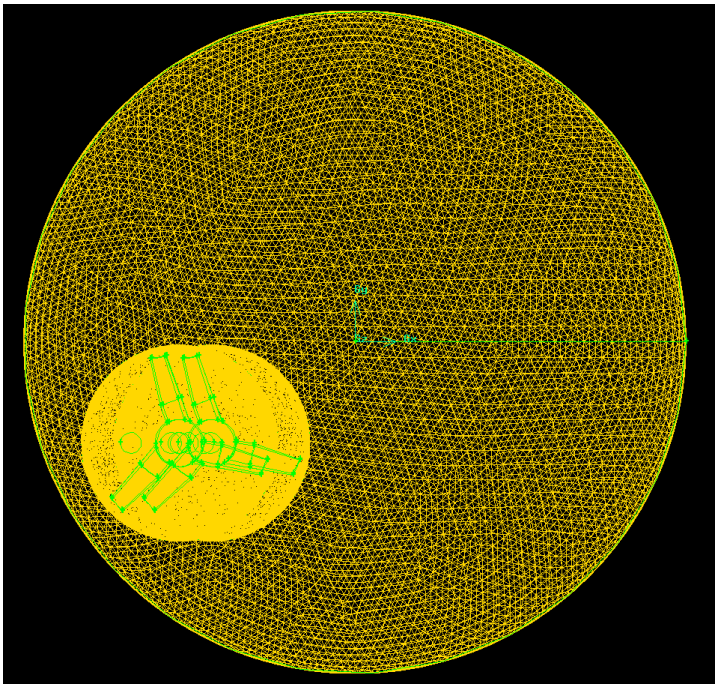

Figure 3.3b Top view of meshing.

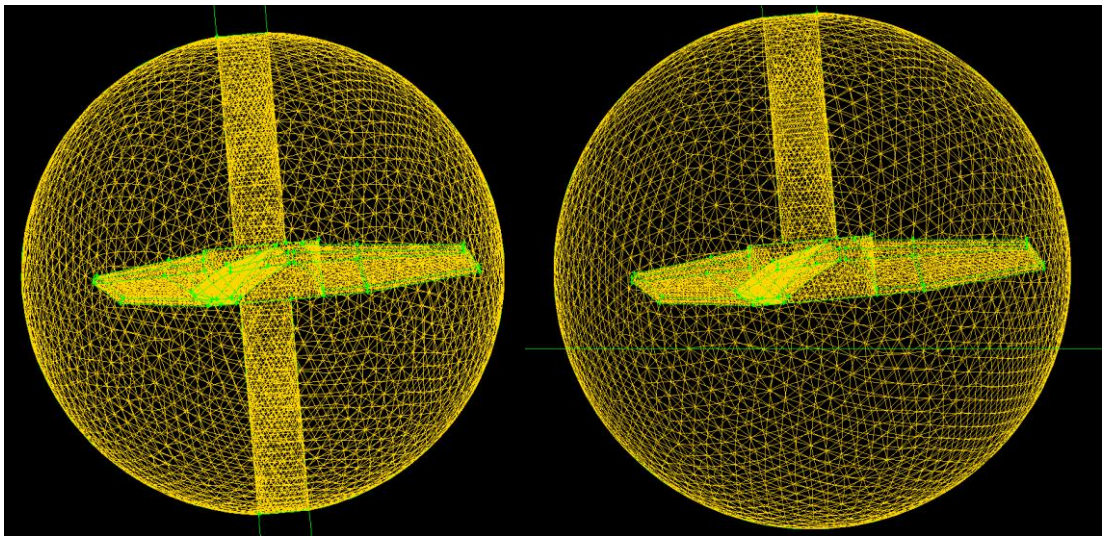

Figure 3.3c Meshing of rotating domain.

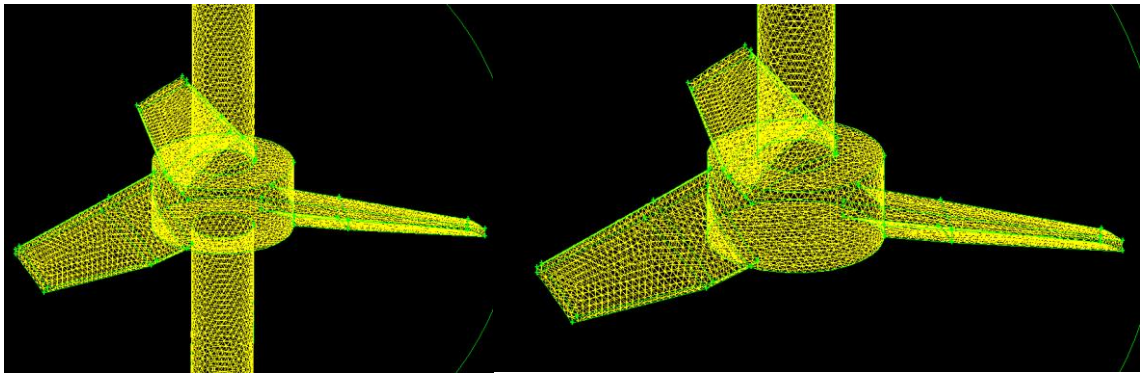

Figure 3.3d Top and bottom impellers meshing with free tetrahedral technique.

3.4 Selection of Turbulence Model for the System under Investigation

As already mentioned, to a mixing vessel, the determination of optimal turbulence model to use in CFD simulations can be made according to equation 3.7, and the conversion of the flow from laminar to turbulence takes place when Reynolds number is 50 to 5000. Therefore, we needed to make sure that the right models are utilized in this study to ensure accurate prediction. In this work simulations were conducted at impeller rotational speeds of 60 rpm, 182 rpm, and 317 rpm, row which Re is respectively 7410.4, 22478.2, and

39151.6. Since off-center, angle-mounted impeller system never been simulated before, the flow regime for the above-mentioned three agitations speeds cannot be assumed to be overall turbulent or not, though the system under three agitation speed conditions can be regarded as the one in the turbulence regime. Therefore it was deemed unwise to apply only one turbulence model. So standard k-ε model, standard k-ω model and a low-Re-number k-ε model, Abid model were chosen to use in the simulation.

3.5 Multiple Reference Frame Method

Multiple reference frame (MRF) applied in this simulation is one of the simplest models to simulate mixing systems. It is a steady-state approximation for the entire domain in a rotating frame by using the momentum equations and the angular velocity of the frame. In this study, the angular velocity of the primary agitation components, directly proportional to the rotational speed of the impellers, was taken as the angular velocity of the frame. So, the volume in the vessel was divided into two reference frames (volumes or domains): the rotating domain and the stationary domain. In the rotating domain, the impellers were assumed to be static, which means that this domain rotates with the impeller. So the momentum equations were solved in the rotating frame while the stationary equations were solved for the stationary domain [14].

A pair of boundaries was created to separate the two domains (Figure 3.10a and 3.10c). The inner volume, or the rotating domain, includes the impeller, while the outer volume contains the rest of the volume in the vessel. When the inner volume was calculated by the equations of motion, the relationship of absolute velocity $\vec{v}$ and the relative velocity $\vec{v}_r$ can be describe as:

$$\vec{v}_r = \vec{v} - \left(\vec{\Omega} \times \vec{r}\right) \tag{3.18}$$

where $\vec{\Omega}$ is the angular velocity vector and $\vec{r}$ is the position of the vector.

For a rotating reference frame, absolute velocity can be toke place by relative velocity $\vec{v}_r$ and the left side of 3.18 can be transferred as:

$$\frac{\partial}{\partial t}(\rho\vec{v}_r) + \nabla \cdot (\rho\vec{v}_r\vec{v}_r) + \rho\left(2\vec{\Omega} \times \vec{v}_r + \vec{\Omega} \times \vec{\Omega} \times \vec{r}\right) + \rho\frac{\partial\vec{\Omega}}{\partial t} \times \vec{r} \tag{3.19}$$

It should be noticed that the Multiple Reference Frame approach does not account for the relative motion of rotation domain and stationary domain. Their grids remain fixed during simulation. This is analogous to freezing the motion of the moving part in a specific position and observing the instantaneous flow field with the rotor in that position. Hence, the MRF is often referred to as the "frozen rotor approach" (FLUENT 6.3 Documentation). At the interface between two domains, the flow in one volume can determine the fluxes of the connected volume, which means the information of the two domains can be exchanged at the boundary. So the MRF approach can be used when the interaction between the two domains is weak or the grids of two domains at the boundary are quite different.

3.6 Boundary Conditions for the System under Investigation

In the CFD simulations, the boundary conditions were defined as following: it was assumed that all solid surfaces have a no-slip conditions; the two-phase air-liquid interface was assumed to be flat and frictionless. This was confirmed by experimental observations of the fluid surface, which showed that even at the highest agitation level (317 rpm) the liquid surface remained practically flat and that the liquid level dropped so little that it can be ignored even when the rotating speed was stopped.

CHAPTER 4

RESULTS

4.1 PIV Results

The results of the PIV experiments are presented in Figures 4.1-4.4 for N=60 rpm, Figures 4.5-4.8 for N=182 rpm, and Figures 4.9-4.12 for N=317 rpm. For each agitation speed the first two figures present the results for Cross Section a1, and the last two figures for Cross Section a2 (Figure 2.8). For each case the first figure presents the experimentally obtained PIV contour plot in which contour lines passing through points with the same velocity intensity are drawn, and the second figure presents the vector fields plot in the same section, colored by vector intensity. Each vector in each figure was the average of 100 PIV measurements. Each figure was obtained by "stitching" together three images, as previous described. Clearly the interfaces between images are not perfectly smooth and can be detected, but such a discontinuity at the interfaces between figures is an artifact of data processing.

These figures show that the flow in the middle section of the vessel (plane a2) is oriented downwards near the center and toward the left of the as a result of the impeller pumping action. However, because of the presence of the hemispherical vessel bottom, the flow reverses its direction in the regions near the wall, where it points upwards. On plane a1 such flow reversal is already complete and the flow is now oriented upwards on nearly the entire portion of cross section observed here. Zones with low velocity can be identified as well in the figures. In particular, some recirculation low-velocity zones can be observed typically between adjacent zones with high velocities but opposite directions where flow recirculation can be expected.

The vectors near the very bottom of the vessel and especially those on the left side appear to be blurred, apparently indicating low velocities. This may actually be caused by the curvature of vessel and by small irregularities in the vessel wall caused by the manufacturing process which become more evident in this region because of the location of the camera: the light scattered by the tracer particles in this region must cross a thicker portion of the vessel wall because of the wall curvature. In addition, some tracer particles typically settled during the PIV measurements and this thin layer further increased the opacity of the vessel bottom from the camera perspective.

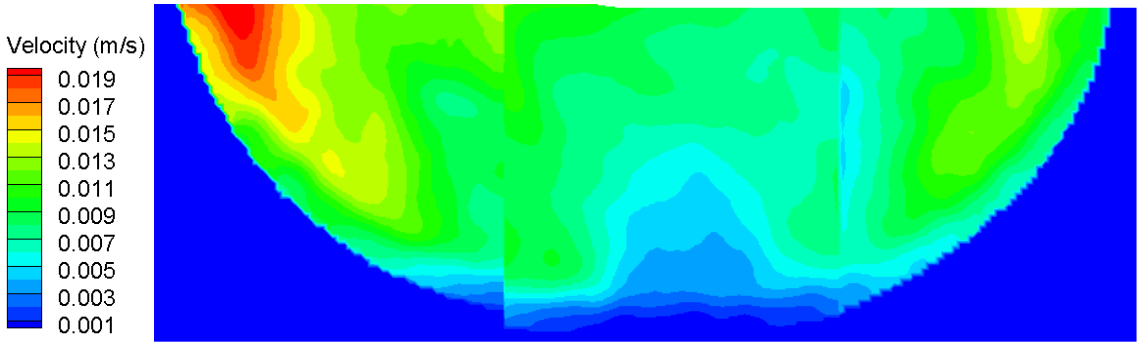

Figure 4.1 Contour plot obtained from PIV data (60 rpm; Plane: a1).

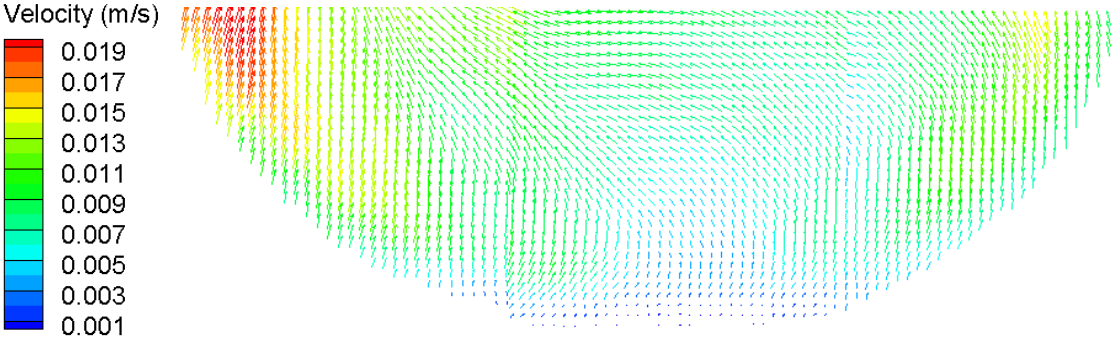

Figure 4.2 Velocity vectors plot obtained from PIV data (60 rpm; Plane: a1).

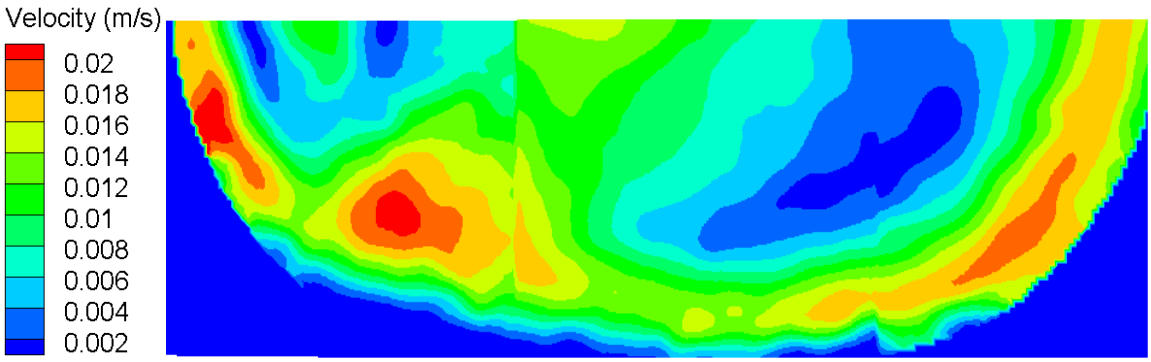

Figure 4.3 Contour plot obtained from PIV data (60 rpm; Plane: a2).

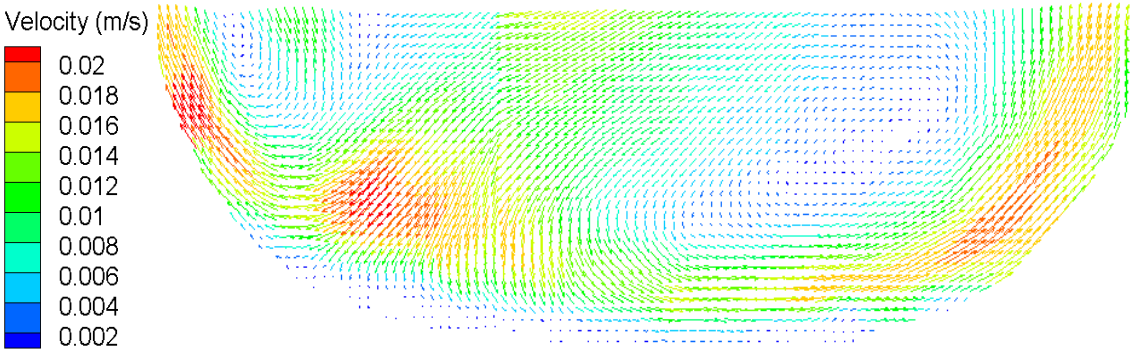

Figure 4.4 Velocity vectors plot obtained from PIV data (60 rpm; Plane: a2).

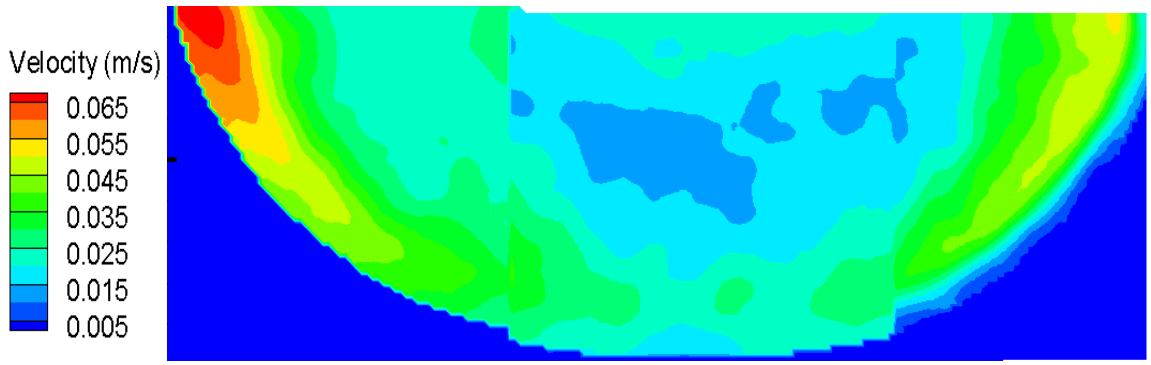

Figure 4.5 Contour plot obtained from PIV data (182 rpm; Plane: a1).

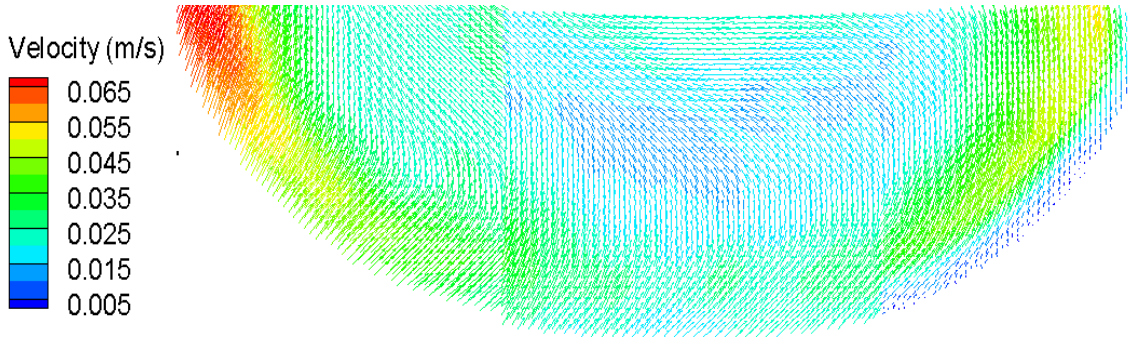

Figure 4.6 Velocity vectors plot obtained from PIV data (182 rpm; Plane: a1).

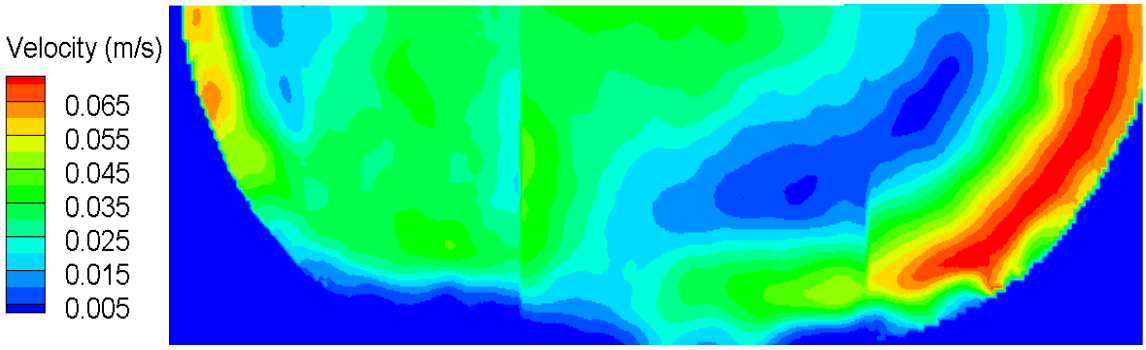

Figure 4.7 Contour plot obtained from PIV data (182 rpm; Plane: a2).

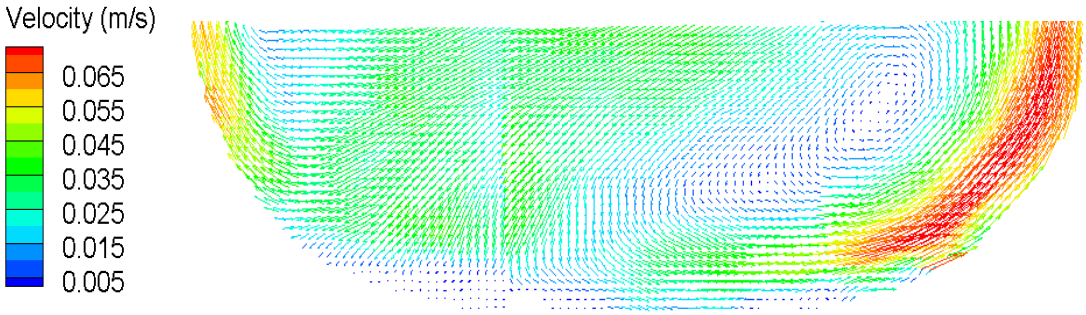

Figure 4.8 Velocity vectors plot obtained from PIV data (182 rpm; Plane: a2).

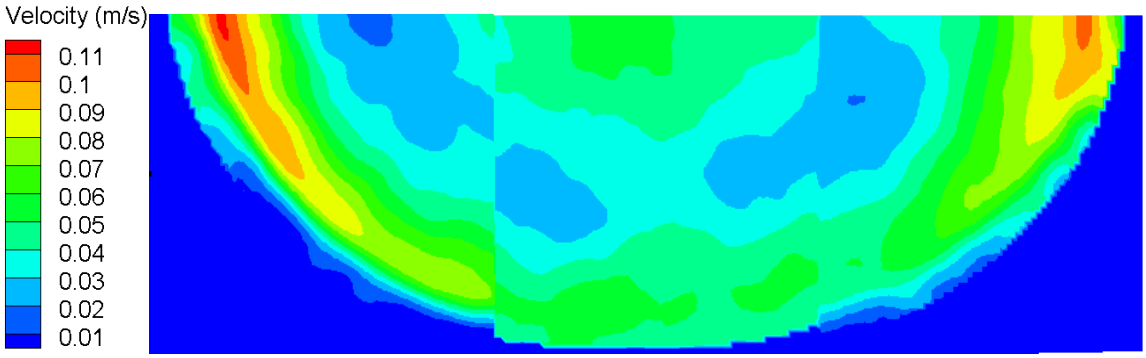

Figure 4.9 Contour plot obtained from PIV data (317 rpm; Plane: a1).

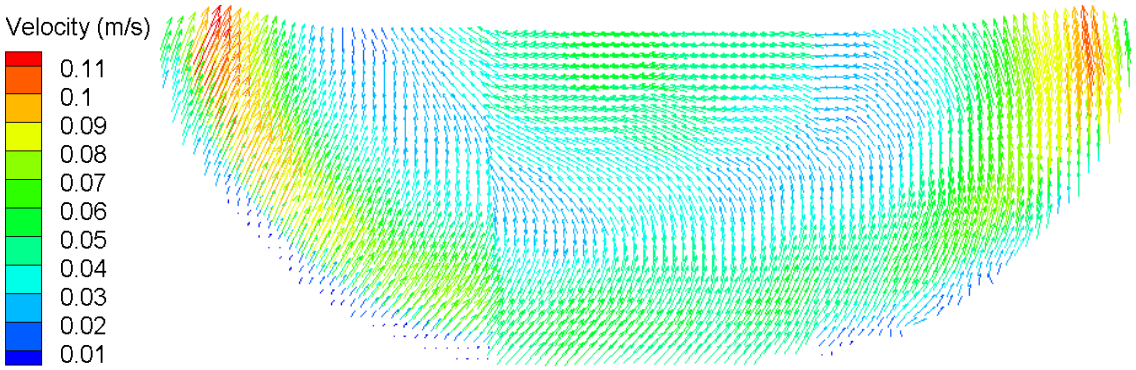

Figure 4.10 Velocity vectors plot obtained from PIV data (317 rpm; Plane: a1).

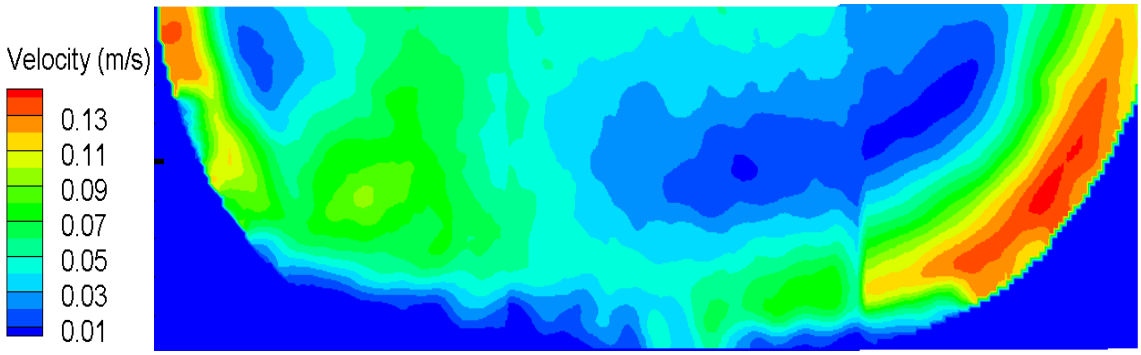

Figure 4.11 Contour plot obtained from PIV data (317 rpm; Plane: a2).

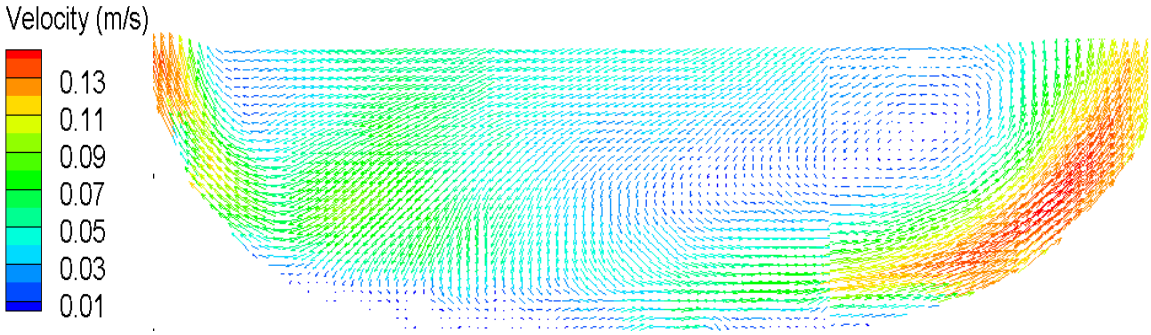

Figure 4.12 Velocity vectors plot obtained from PIV data (317 rpm; Plane: a2).

4.2 Result of CFD simulation

The CFD simulations were conducted at the same three agitation speeds used in the PIV experiments (60 rpm, 182 rpm, and 317 rpm). For each simulation condition, the images of contours plots and the images of vector of velocity were obtained. In each figure in Figures 4.13-4.18 the contours plots for simulation conducted with different turbulent models (standard k-ε model, k-ω model, and the low Reynolds number k-ε model, Abid model) are reported. Results for both plane a1 and plane a2 are shown in different figures.

These figures indicate that the pattern and strength of the flows simulated by standard k-ε model and low-Re-number k-ε model are similar: for example, despite some relatively small differences, they both show a vortex in the center of the upper part of plane a2 and a small vortex in the bottom of the vessel so that two main circulations in lower part and upper part are formed. On the other hand, the simulation results with the standard k-w model tell a different story. The vortex in the bottom is so small that partial circulation in the bottom can be ignored. These predictions show there are many small vortex centers in the upper part of vessel, which means the flow simulated with the standard k-ω is predicted to be more complex than the flows predicted by the other two models.

In order to determine which model better predicted the experimental result, a comparison with the experimental PIV data was made, as reported in the next chapter.

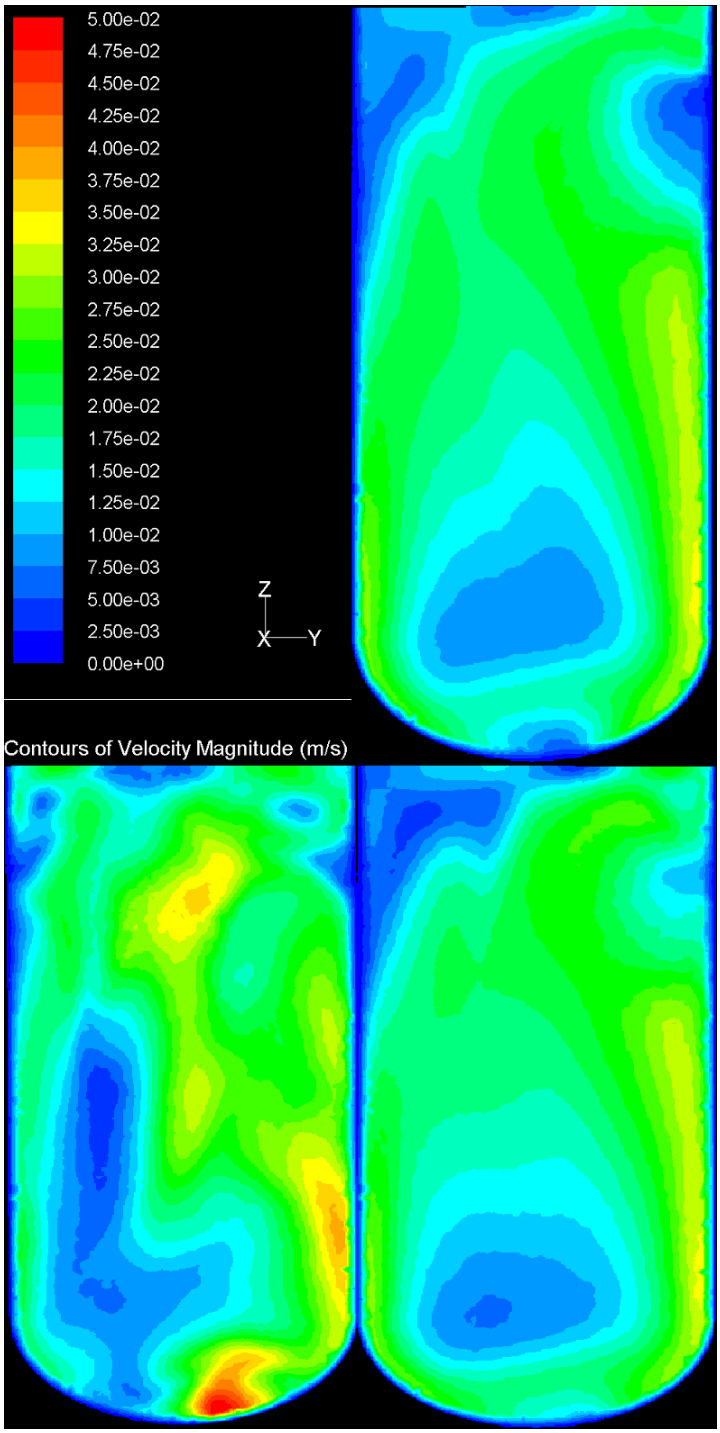

Figure 4.13 CFD predicted contours of velocity magnitude on Plane a1 (N=60 rpm) obtained using different turbulence models: velocity color scale (top left); standard k-ε model (top right), k-ω model (bottom left); Abid model (bottom right).

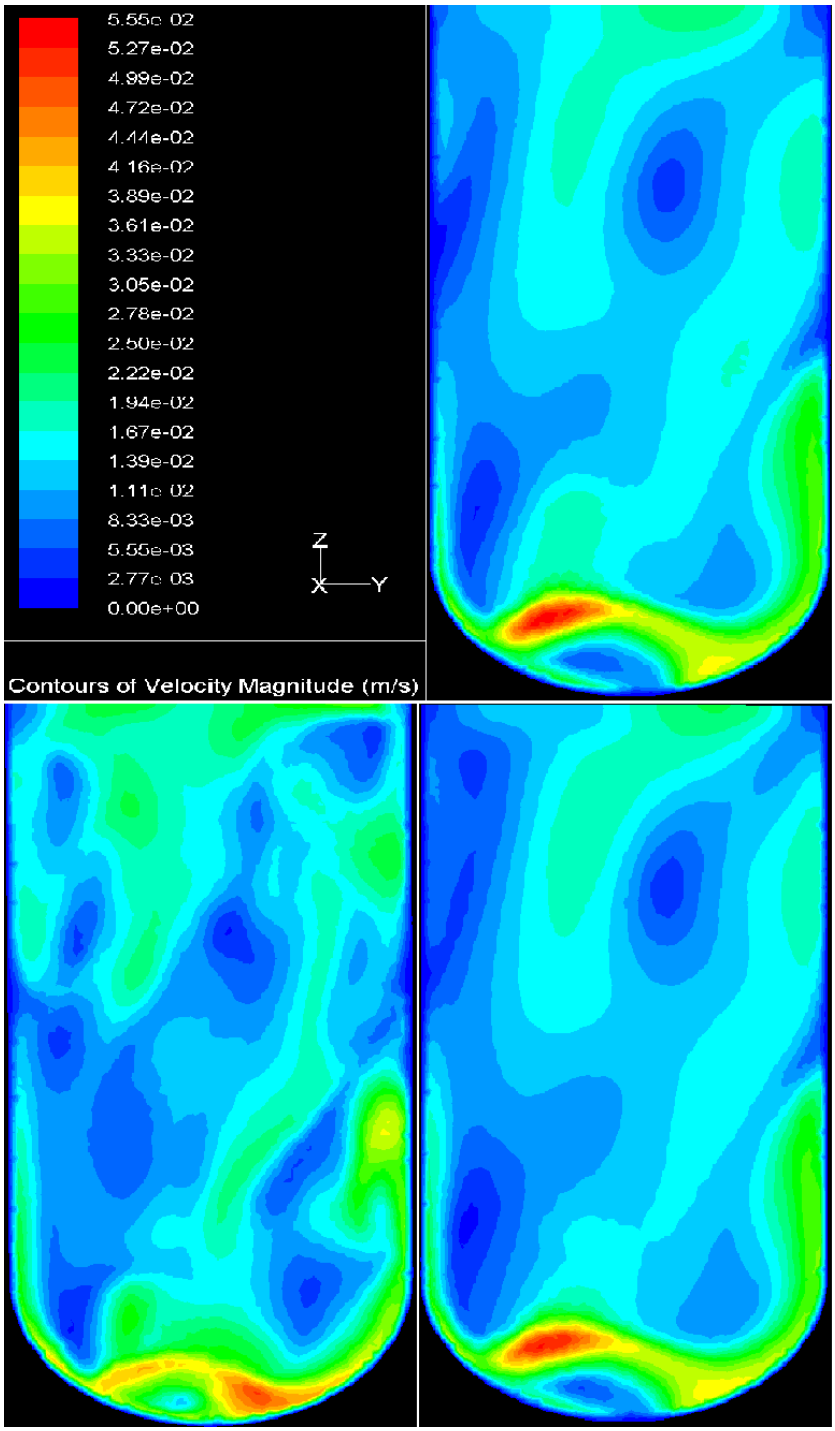

Figure 4.14 CFD predicted contours of velocity magnitude on Plane a2 (N=60 rpm) obtained using different turbulence models: velocity color scale (top left); standard k-ε model (top right), k-ω model (bottom left); Abid model (bottom right).

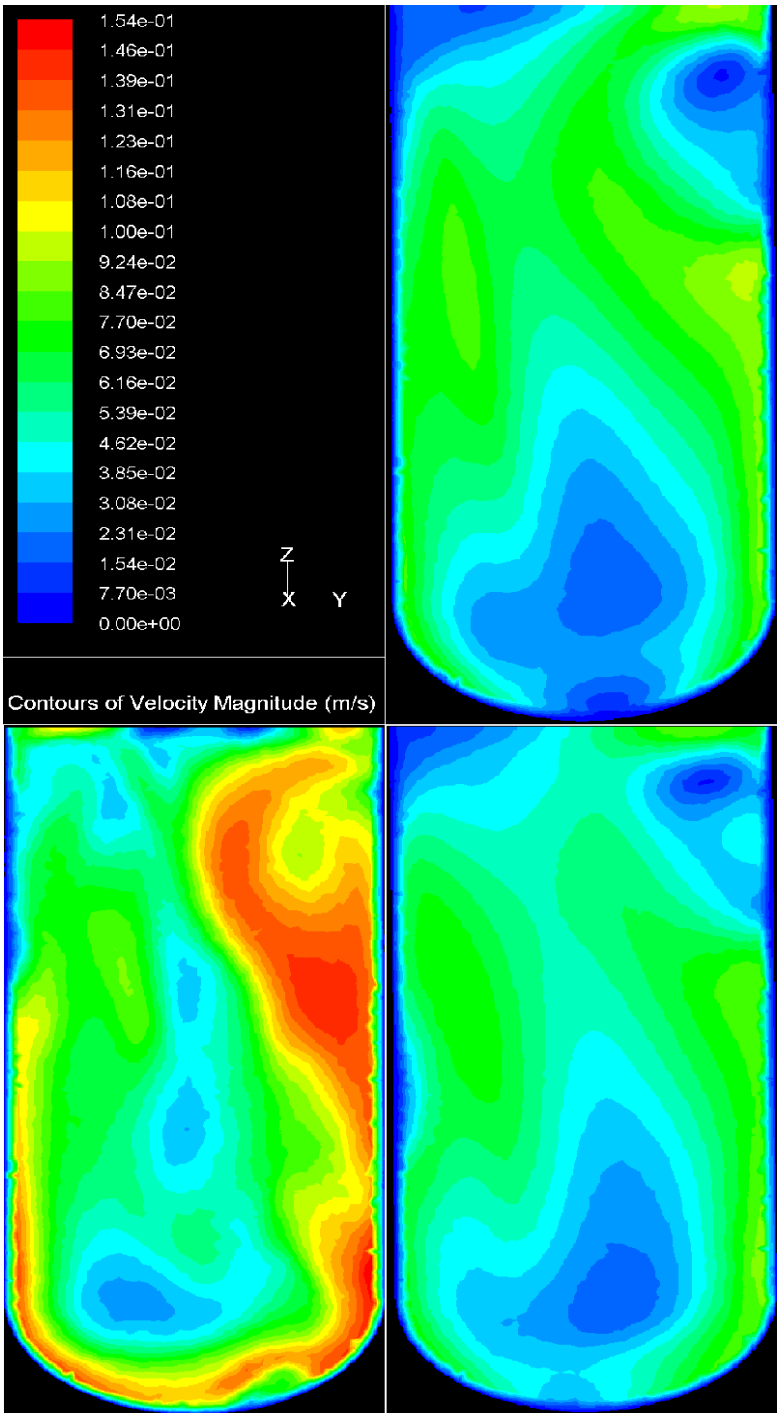

Figure 4.15 CFD predicted contours of velocity magnitude on Plane a1 (N=182 rpm) obtained using different turbulence models: velocity color scale (top left); standard k-ε model (top right), k-ω model (bottom left); Abid model (bottom right).

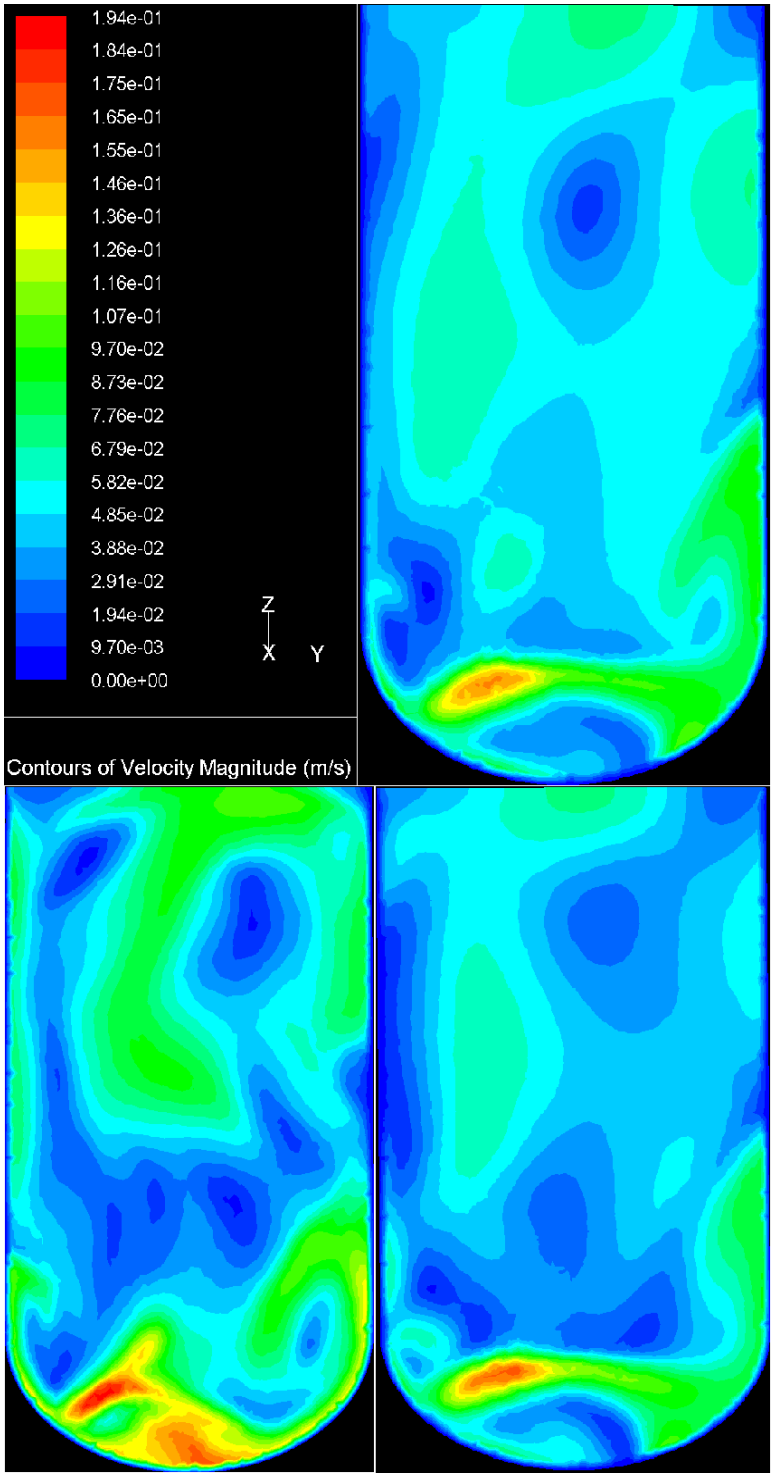

Figure 4.16 CFD predicted contours of velocity magnitude on Plane a2 (N=182 rpm) obtained using different turbulence models: velocity color scale (top left); standard k-ε model (top right), k-ω model (bottom left); Abid model (bottom right).

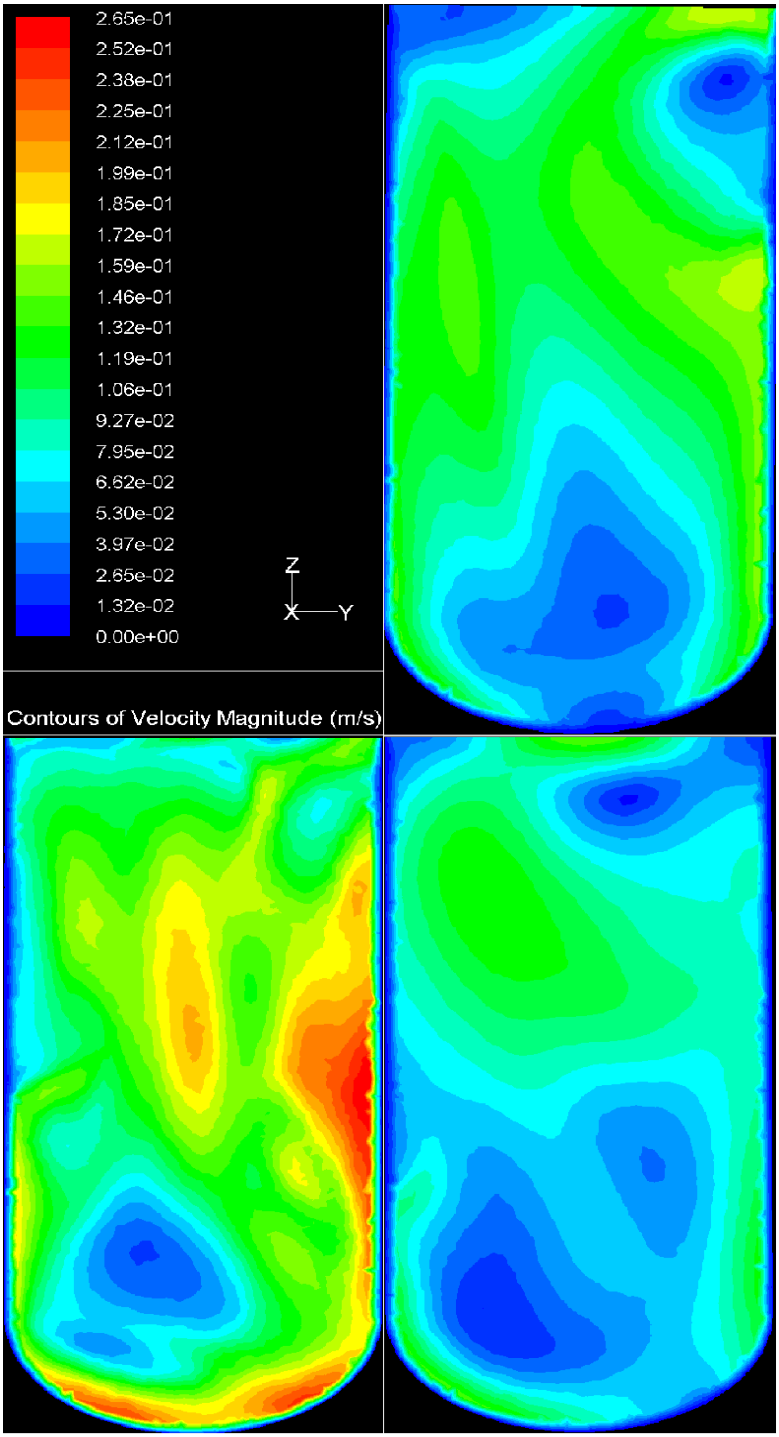

Figure 4.17 CFD predicted contours of velocity magnitude on Plane a1 (N=317 rpm) obtained using different turbulence models: velocity color scale (top left); standard k-ε model (top right), k-ω model (bottom left); Abid model (bottom right).

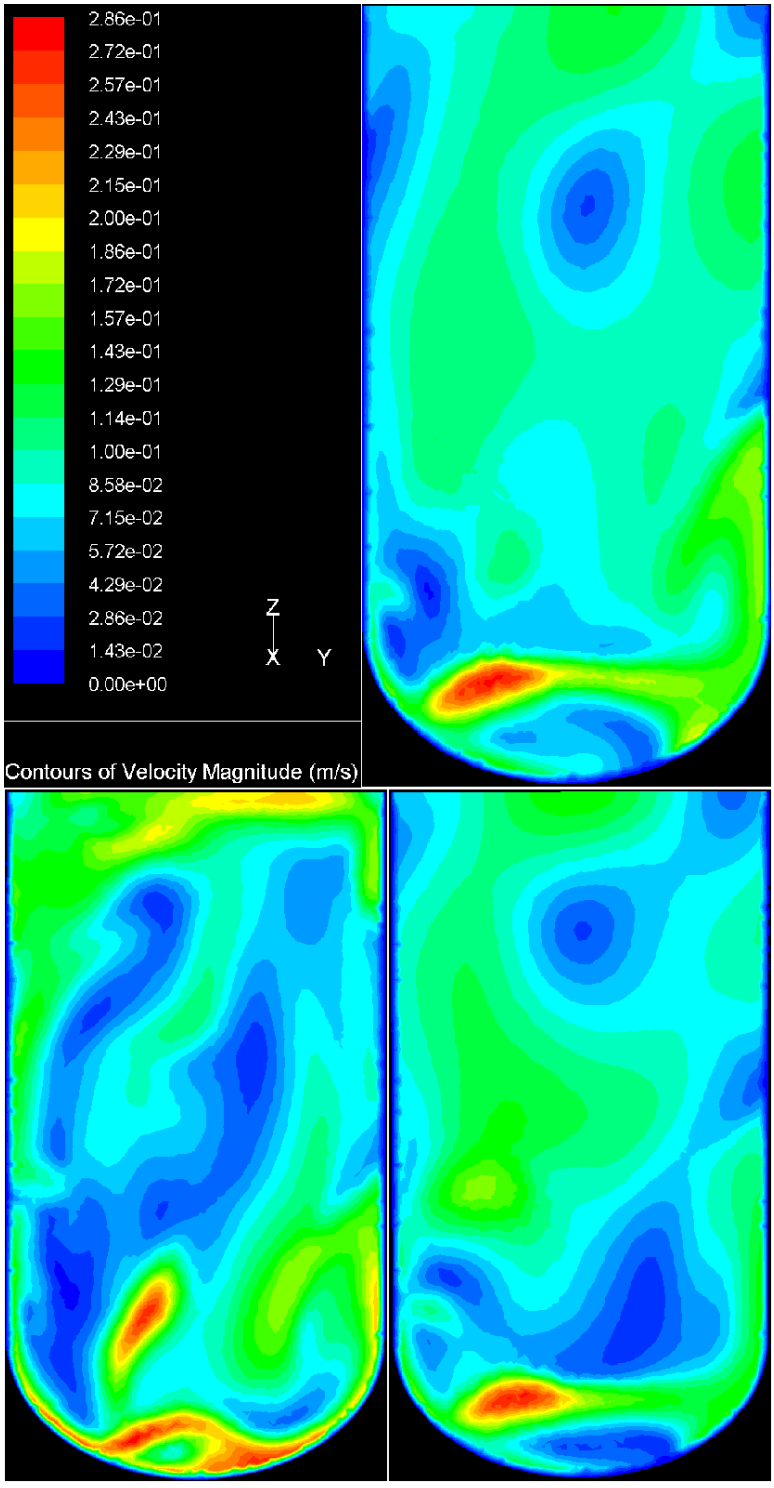

Figure 4.18 CFD predicted contours of velocity magnitude on Plane a2 (N=317 rpm) obtained using different turbulence models: velocity color scale (top left); standard k-ε model (top right), k-ω model (bottom left); Abid model (bottom right).

CHAPTER 5

COMPARISON BEWTEEN PIV AND CFD RESULTS AND DISCUSSION

An overall comparison between the PIV results and the CFD predictions shows that, in general, there is an apparent agreement between the experimental results and the predictions obtained with the k-ε model and the low-Re-number k-ε model, but not with the k-ω model. So, further comparisons with the results with the *k*-ω model was not considered.

There is an important point to be made before comparisons can be made: the results of the PIV experiments are two-dimensional, while the CFD predictions are three-dimensional. Therefore, the CFD predictions were used here to generate two-dimensional CFD vector plots in which the velocity projections on the plane a1 and a2 were obtained. This enables proper comparisons between PIV results and CFD predictions to be made.

Comparisons between the PIV results and the CFD simulations obtained with the k-ε model and the low-Re-number k-ε model are shown in Figures 5.1-5.6. As one can see in Figure 5.1 and Figure 5.2, the results obtained at 60 rpm show substantial agreement between experiments and predictions. Qualitative agreement is also visible at the other two agitation speeds, although the quantitative agreement is less satisfactory. The largest difference is the high velocity region (large red area) in the center-left of Cross Section a2, which is under the lower end of shaft and the flow generated by the lower A-310 impellers is mainly responsible for it.

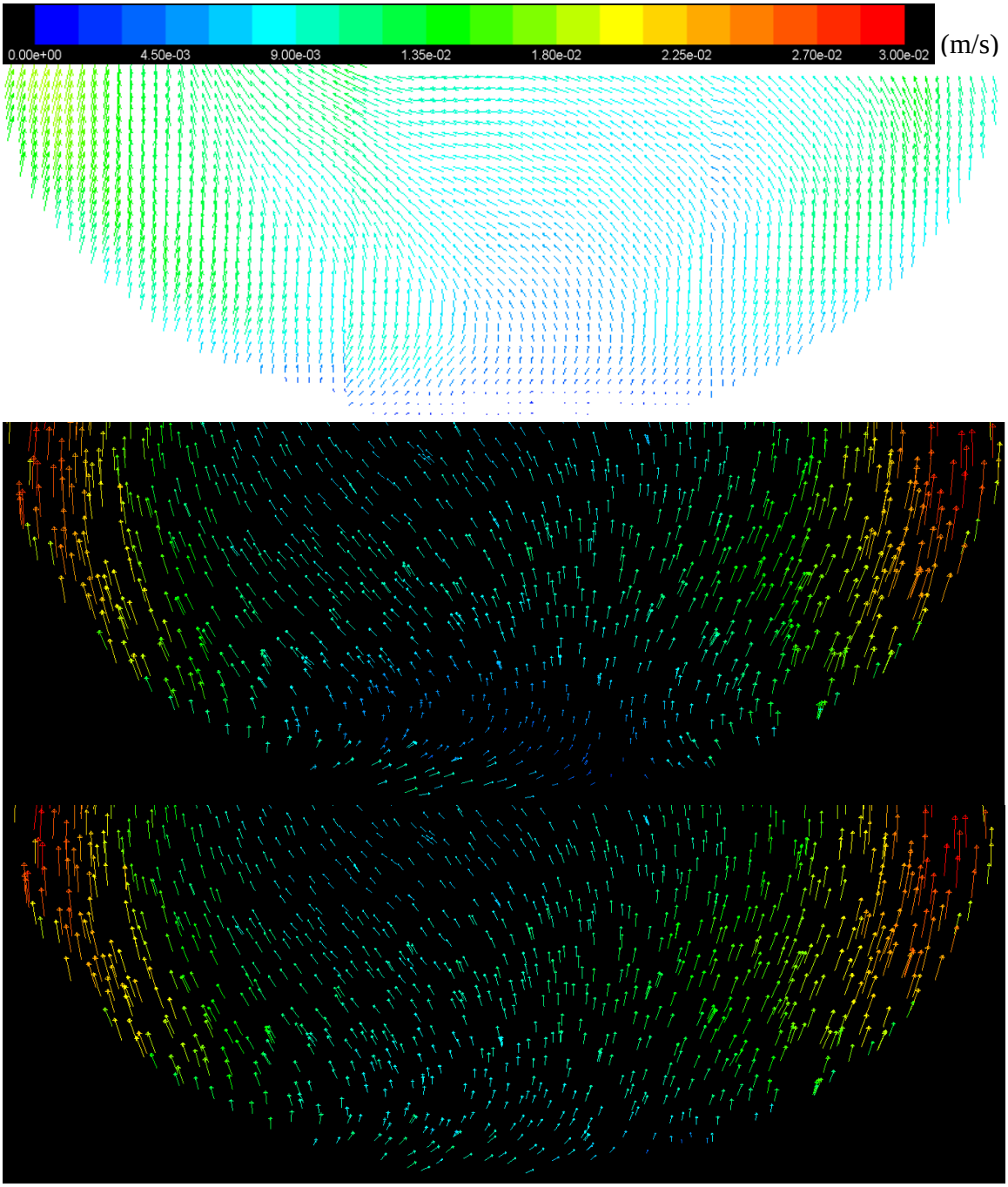

Figure 5.1 Velocity vectors at 60 rpm on plane a1: PIV results (top), CFD prediction with standard *k*-ε model (middle) and Abid model (bottom).

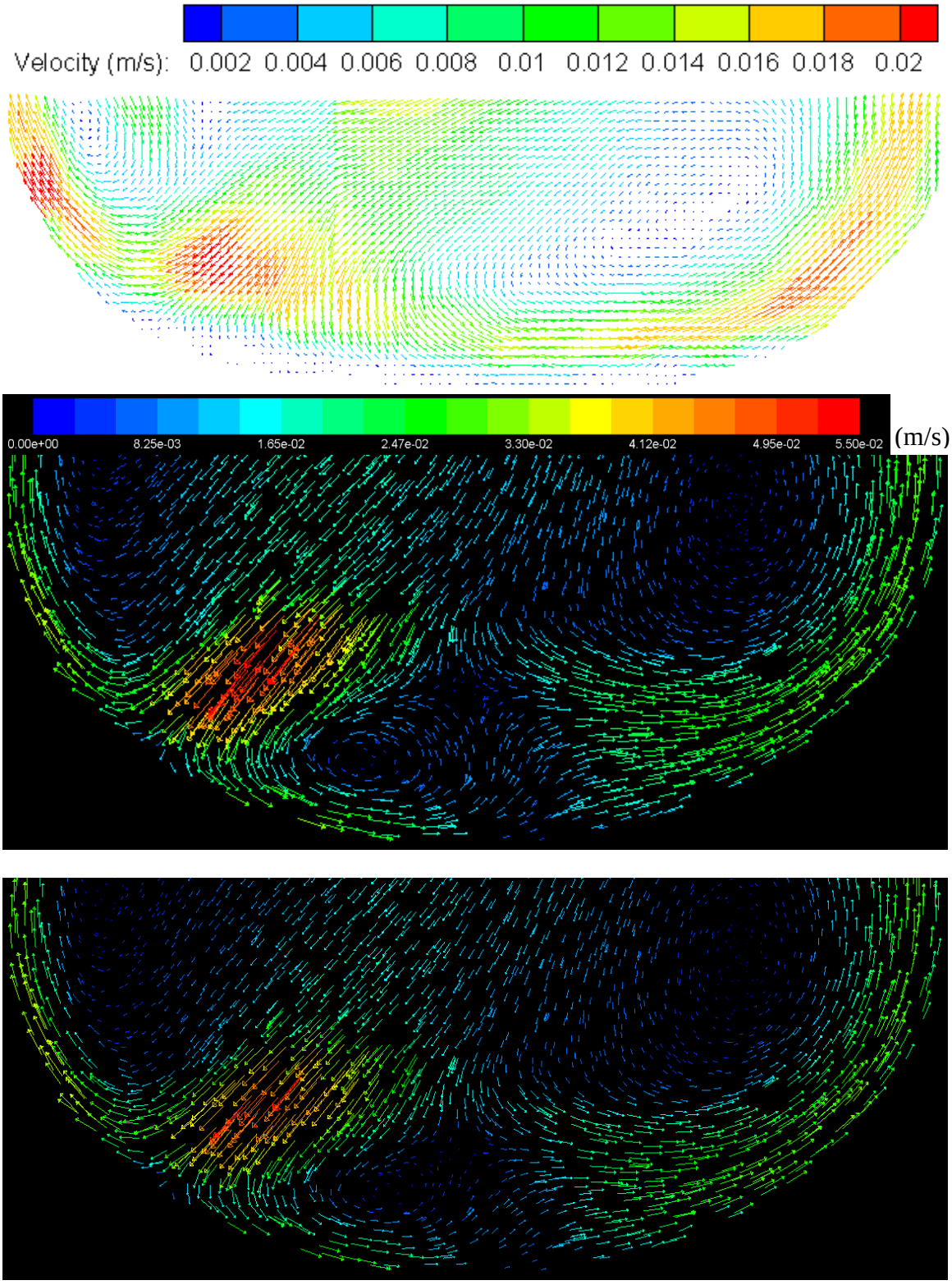

Figure 5.2 Velocity vectors at 60 rpm on plane a2: PIV results (top), CFD prediction with standard *k*-ε model (middle) and Abid model (bottom).

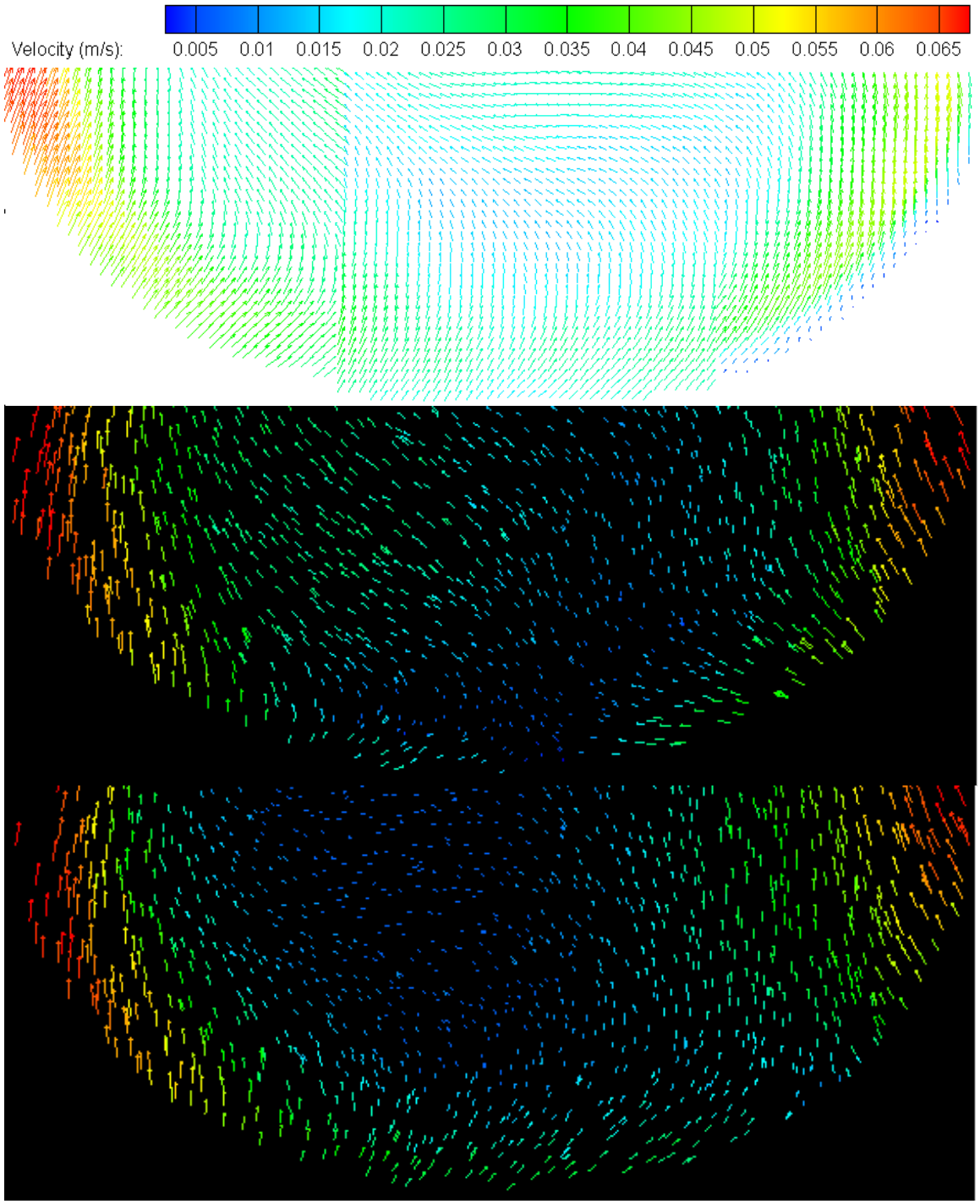

Figure 5.3 Velocity vectors at 182 rpm on plane a1: PIV results (top), CFD prediction with standard *k*-ε model (middle) and Abid model (bottom).

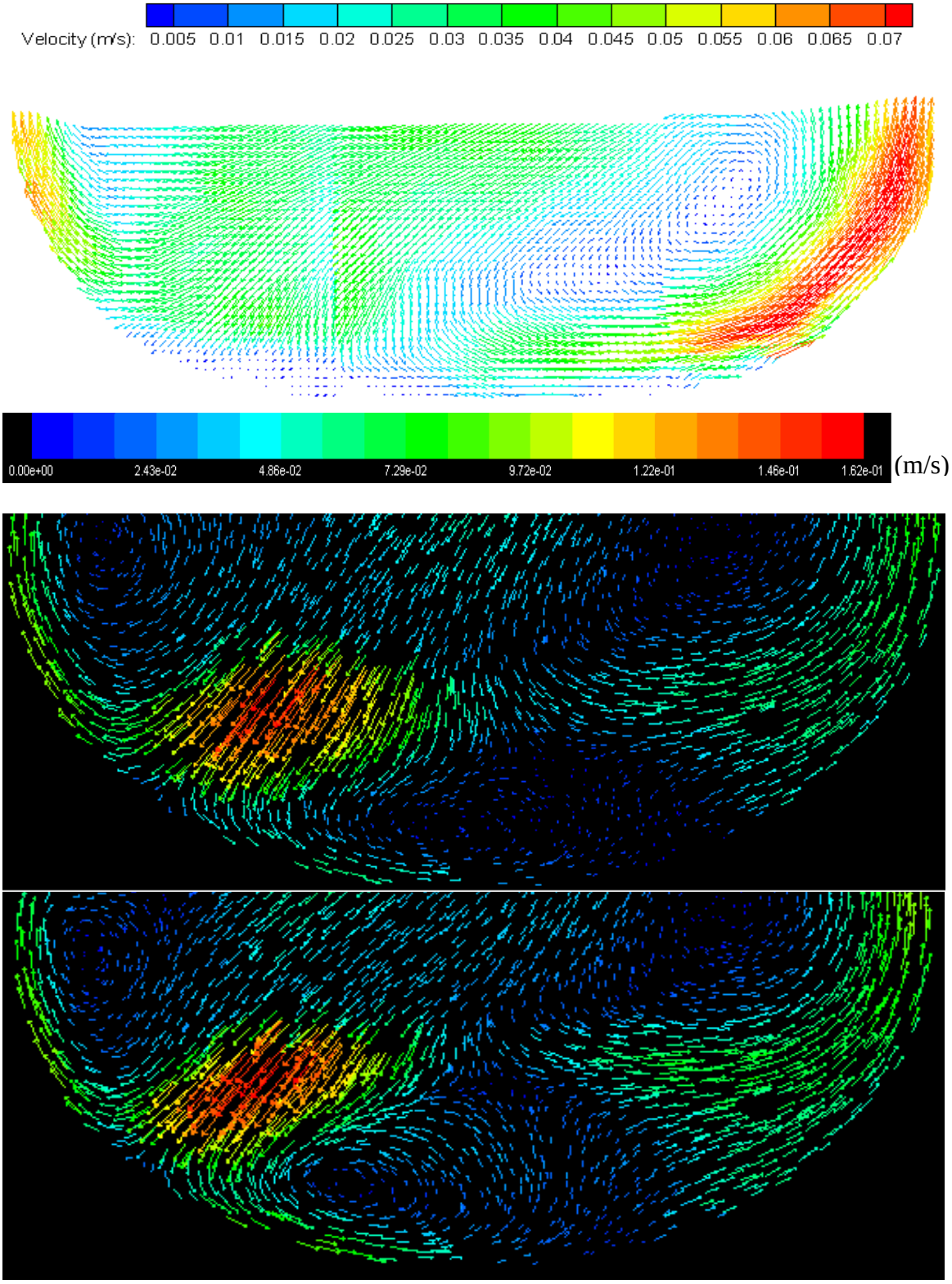

Figure 5.4 Velocity vectors at 182 rpm on plane a2: PIV results (top), CFD prediction with standard *k*-ε model (middle) and Abid model (bottom).

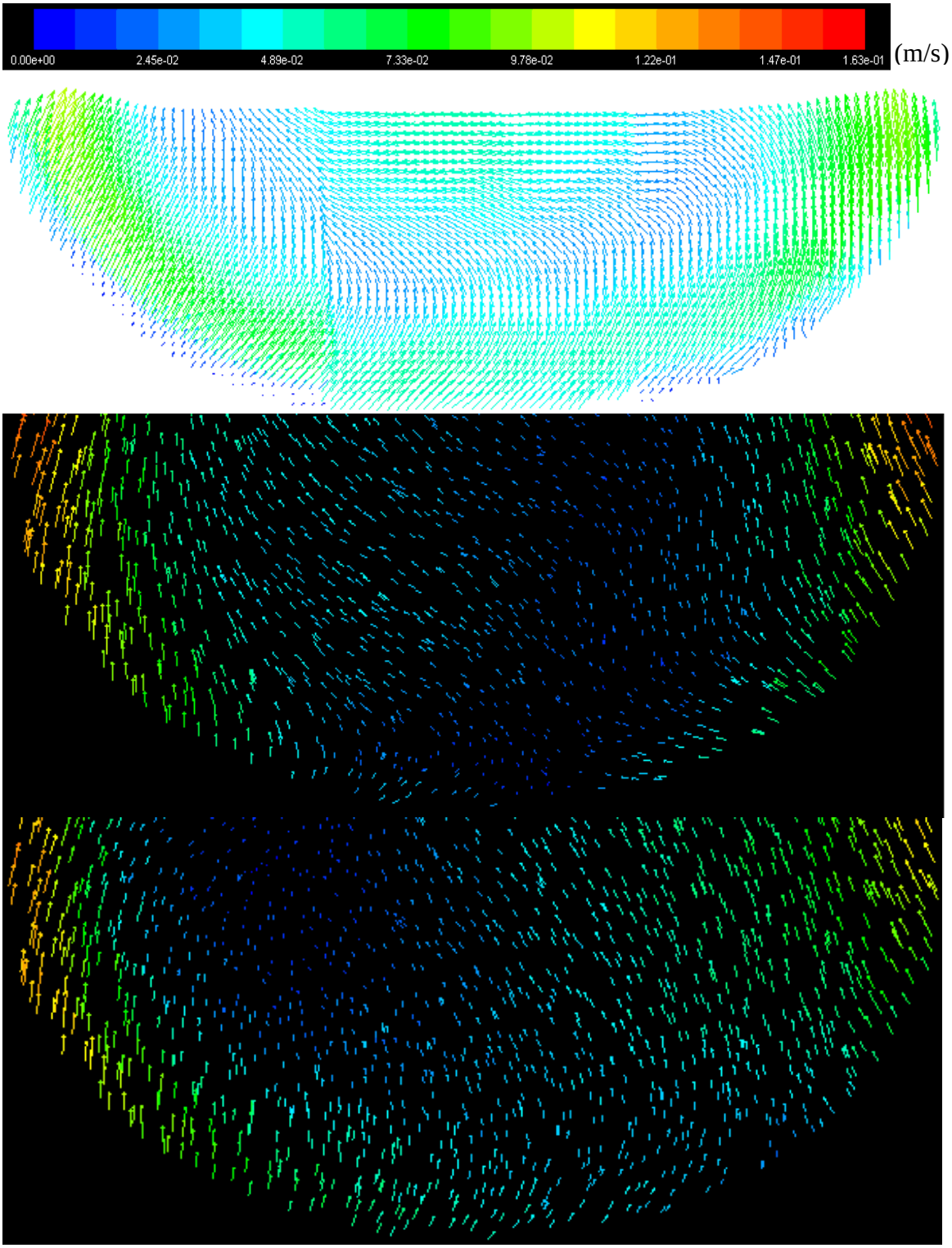

Figure 5.5 Velocity vectors at 317 rpm on plane a1: PIV results (top), CFD prediction with standard *k*-ε model (middle) and Abid model (bottom).

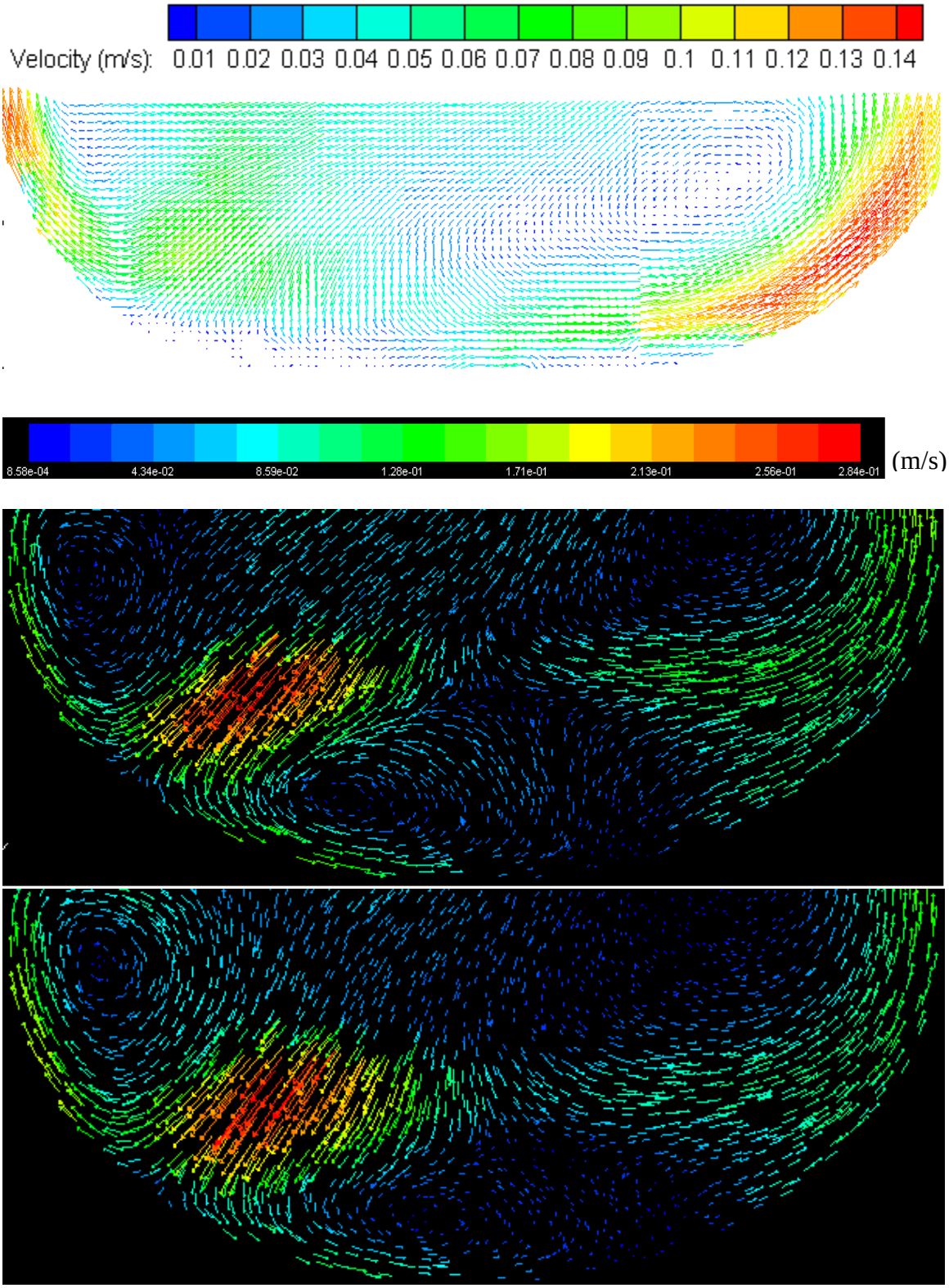

Figure 5.6 Velocity vectors at 317 rpm on plane a2: PIV results (top), CFD prediction with standard *k*-ε model (middle) and Abid model (bottom).

The A-310 impeller generates an axial flow, and this is evident from the PIV results. However, as shown in Figure 5.7, the flow generated by the top impeller appears to change depending on the agitation speed, according to the CFD simulation.

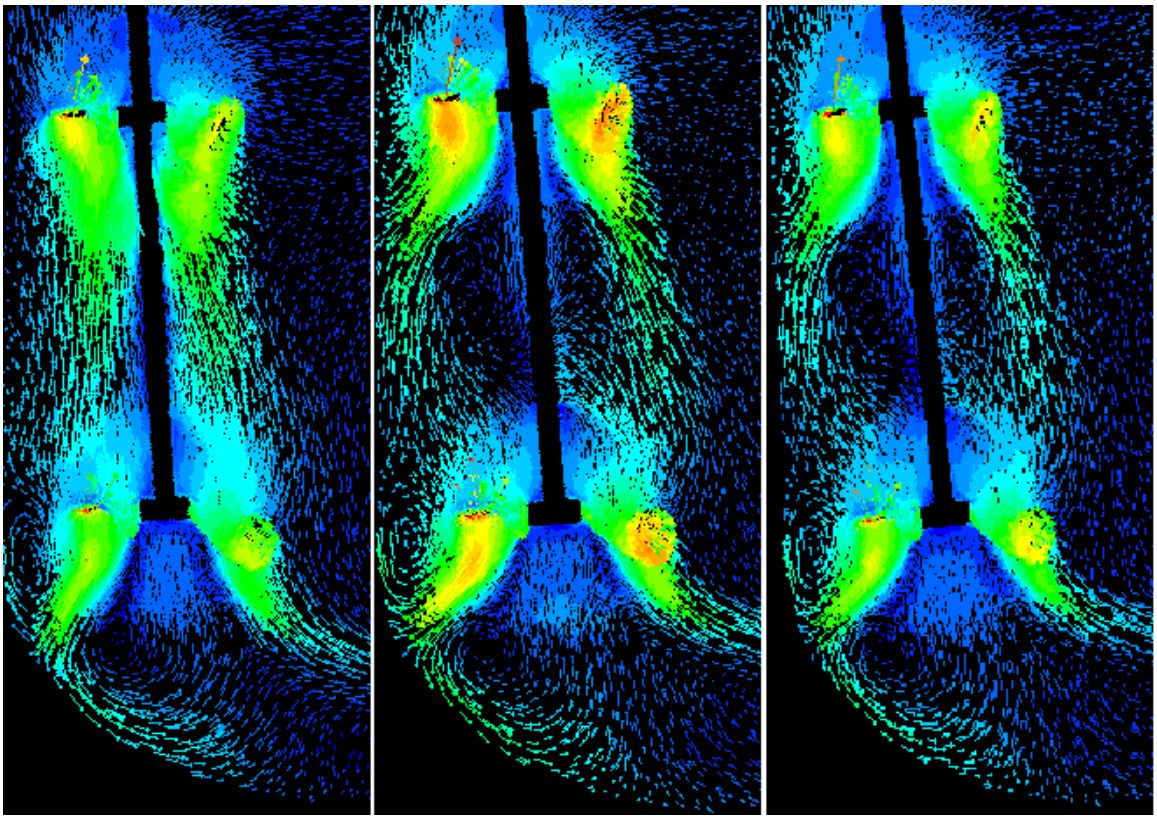

Figure 5.7 CFD profiles of flow on a plane through the shaft (scale adjusted) at 60 rpm (left panel), 182 rpm (center panel), and 317 rpm (right panel).

It happens because Fluent 6.3.26 with k-ε model consider the pressure change to be a very important factor which can take a big influence on the fluid. It is reasonable that as the rotation speed increases, the change of pressure from the center of impeller to the ending point of blades becomes larger. It is similar to the shaft and volume around it that bigger gap of velocity increases the gap of pressure, and the gradient of pressure cause the tendency of the flow and vortex. But according to the result illustrated in 5.7, the effect of

the pressure seems not as important as what it is thought to be. There are also many factors that may causes these differences, such as impeller modeling and the approach of MRF. Figure 5.8 is a close-up image which belongs to the plane next to the impeller. This plane is parallel to plane a1, -97.5mm away from plane a2. The impeller can be seen to generate a downward pumping action. Then the vortex generated by pressure difference, changes the direction of the flow and increases the radial component.

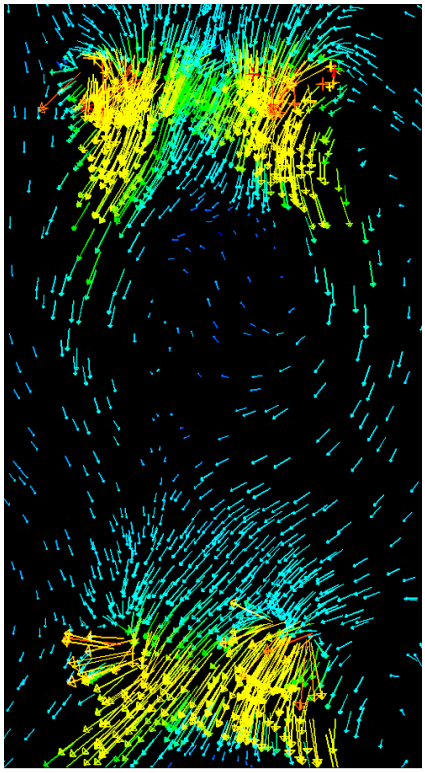

Figure 5.8 Close-up image of upper impeller. Scale adjusted, brightness +60%.

In the previous studies by our group a comparison of the CFD and PIV results was often generated. In the present case however, the complexity and the non-symmetric three-dimensional flow makes this comparison quite difficult. Therefore, here a comparison was made by identifying locations in similar regions that exhibited similar qualitative flow behaviors. Then the PIV and CFD velocities at those locations were

compared. Specifically, three locations on Cross Section a1 were selected (A, B and C) as shown in Figure 5.9. Similarly, five locations on Cross Section a2 were selected (A, B, C, D and E). At each one of these locations the PIV-measured velocities and the corresponding CFD-predicted velocities were compared (Figure 5.9).

In plane a1, Locations A and C are in the high velocity region close to the wall of vessel, and Location B represent the points near the bottom. In Cross Section a2, Locations A and E are in the high velocity region close to the wall, while Locations B and D are the in the slower regions where recirculation vortexes can be seen. Because of the higher velocity in the center-left, Location C in Cross Section a2 was also selected.

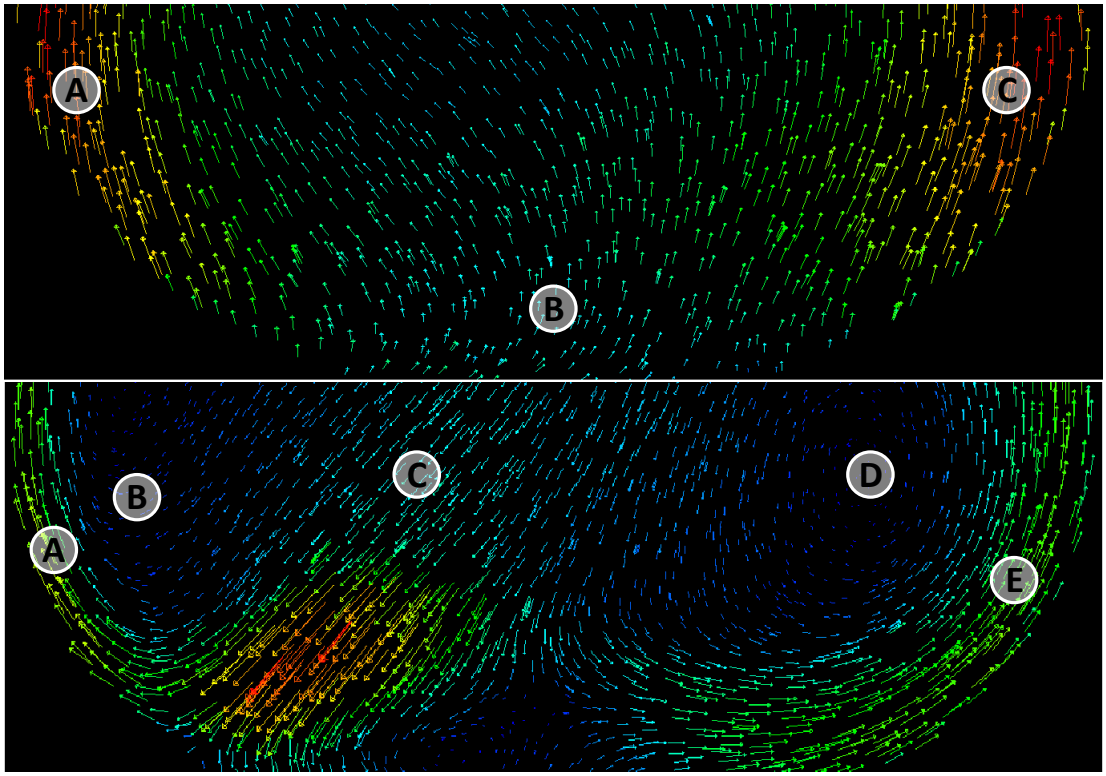

Figure 5.9 Selected points were comparisons between PIV-measure velocities and the corresponding CFD-predicted velocities were made: Cross Section a1 (upper panel) and Cross Section a2 (lower panel).

The results are shown in Tables 5.1 (60 rpm), Tables 5.2 (182 rpm), and Tables 5.3 (317 rpm). Comparisons are provided for the actual absolute magnitude of the velocity (L), as well as velocity components in the vertical direction (V) and horizontal direction (U). The results indicate that the CFD-predicted velocity using both the standard k-ε and the low Re k-ε model are, in general, in substantial agreement with the PIV measurements.

According to tables, both standard k-ε model and Abid model basically reflect the experimental situation. It is seems that the low-Re-number k-ε model, Abid model, attend to make a more balanced prediction than standard k-ε model. Abid model predicts higher velocity volume in low speed regions while the standard k-ε model gives better predictions in the higher velocity region. As the increase of agitation speed, the Reynold number increases as well, and the results of the standard *k*-ε model at 317 rpm are in closer agreement with the results of the PIV.

Table 5.1 Comparison between PIV measurements and the CFD-predictions of velocities at selected locations on plane a1 and a2 at N=60 rpm. L: Absolute magnitude of the velocity; V: velocity components in the vertical direction; U: velocity component in the horizontal direction (U)

Results for Agitation Speed = 60 rpm					
Plane	Location	Method	Velocity (mm/s)		
			Direction		
			L	U	V
a1	A	*PIV*	20.17	4.73	19.61
		CFD-k-ε	22.13	2.97	21.92
		Abid	24.28	0.79	24.27
	B	*PIV*	4.12	-1.19	3.94
		CFD-k-ε	5.24	1.53	4.96
		Abid	8.65	2.23	8.34
	C	*PIV*	14.27	-4.29	13.61
		CFD-k-ε	24.31	-1.69	24.25
		Abid	16.23	-0.69	16.2
a2	A	*PIV*	20.97	-11.16	17.75
		CFD-k-ε	20.45	-7.41	19.04
		Abid	22.76	-3.96	22.4
	B	*PIV*	4.79	-3.15	-3.61
		CFD-k-ε	5.83	-5.49	-0.58
		Abid	4.44	-3.93	-1.71
	C	*PIV*	12.87	-11.94	-4.81
		CFD-k-ε	18.49	-13.19	-12.9
		Abid	15.31	-10.23	-11.39
	D	*PIV*	2.31	-2.15	-0.84
		CFD-k-ε	2.41	-2.19	-0.93
		Abid	4.57	-3.5	-2.88
	E	*PIV*	19.18	15.1	11.82
		CFD-k-ε	26.73	7.7	25.59
		Abid	25.58	4.17	25.23

Table 5.2 Comparison between PIV measurements and the CFD-predictions of velocities at selected locations on plane a1 and a2 at N=182 rpm. L: Absolute magnitude of the velocity; V: velocity components in the vertical direction; U: velocity component in the horizontal direction (U)

Results for Agitation Speed = 182 rpm					
Plane	Location	Method	Velocity (mm/s)		
			Direction		
			L	U	V
a1	A	*PIV*	66.61	23.97	62.15
		CFD-k-ε	66.91	13.51	65.51
		Abid	67.01	20.59	63.77
	B	*PIV*	21.94	10.02	19.52
		CFD-k-ε	20.04	-17.17	-8.69
		Abid	20.19	10.29	17.35
	C	*PIV*	48.94	4.45	48.93
		CFD-k-ε	55.7	-21.10	51.55
		Abid	42.92	16.01	39.74
a2	A	*PIV*	62.24	-31.85	53.48
		CFD-k-ε	55.93	-18.17	52.83
		Abid	71.87	-12.82	70.72
	B	*PIV*	14.35	-13.71	4.21
		CFD-k-ε	16.89	-15.85	3.81
		Abid	22.62	-21.91	2.68
	C	*PIV*	34.56	-32.27	-12.1
		CFD-k-ε	34.03	-24.79	-23.31
		Abid	38.53	-19.36	-33.30
	D	*PIV*	6.38	-3.91	-5.04
		CFD-k-ε	12.35	-6.57	-10.17
		Abid	10.78	-4.74	-9.38
	E	*PIV*	73.94	55.23	55.34
		CFD-k-ε	80.07	13.41	78.89
		Abid	66.61	23.97	62.15

Table 5.3 Comparison between PIV measurements and the CFD-predictions of velocities at selected locations on plane a1 and a2 at N=317 rpm. L: Absolute magnitude of the velocity; V: velocity components in the vertical direction; U: velocity component in the horizontal direction (U)

Results for Agitation Speed = 317 rpm					
Plane	Location	Method	Velocity (mm/s)		
			Direction		
			L	U	V
a1	A	*PIV*	108.7	46.15	98.4
		CFD-k-ε	123.01	22.75	107.32
		Abid	94.53	17.91	85.05
	B	*PIV*	54.21	34.52	41.8
		CFD-k-ε	50.46	21.41	45.69
		Abid	56.64	-6.63	37.13
	C	*PIV*	102.6	-18.8	100.9
		CFD-k-ε	95.45	-28.91	78.53
		Abid	104.88	-35.9	70.02
a2	A	*PIV*	131.2	-35.36	126.4
		CFD-k-ε	144.15	-62.79	106.37
		Abid	151.38	-55.18	140.96
	B	*PIV*	16.8	-16.43	3.48
		CFD-k-ε	24.62	-20.14	10.56
		Abid	27.81	-18.38	20.87
	C	*PIV*	67.25	-61.71	-26.73
		CFD-k-ε	49.94	-39.58	-42.87
		Abid	53.07	-24.48	-44.67
	D	*PIV*	9.27	-2.36	-8.96
		CFD-k-ε	28.81	24.56	-14.24
		Abid	14.08	8.97	-10.85
	E	*PIV*	143.8	99.09	104.2
		CFD-k-ε	140.03	30.36	136.53
		Abid	108.7	46.15	98.4

CHAPTER 6

CONCLUSION

In this work the hydrodynamics of water as a model fluid was studied both computationally and experimentally in a scaled down version of an industrial vessel with an elliptical bottom and provided with two angle-mounted fluidfoil impellers. The system was operated under different operating conditions in order to replicate the mixing characteristics of the industrial system. A number of conclusions can be drawn from the results obtained here:

1. The CFD results obtained when the standard *k*-ε model or the low Reynolds number *k*-ε model (Abid model) were used to simulate turbulence effects were very similar and, typically, in significant quantitative agreement with each other. However, the results obtained with the standard k-ω model for turbulence were appreciably different from the results obtained with the other two models;
2. The experimentally obtained PIV velocity distributions on two vertical planes, labeled "Plane a1" and "Plane a2", both in the lower portion of the vessel, were in close overall agreement with the CFD results obtained with the standard *k*-ε model or the low Reynolds number *k*-ε model. Quantitative comparison at a number of locations within the vessel also showed substantial agreement;
3. Based on these results, the MRF approach used in the CFD simulations appears to be appropriate to capture the flow in the system under investigation;
4. Because of the asymmetric angled position of the impellers, the flow in the vessel is highly complex. The results show that the primary downward flow generated by the impellers reaches approximately the bottom hemispherical bottom of the vessel

and then generate an upward fluid movement near the wall. Several less well mixed recirculation regions can be identified in the vessel. Of special relevance is the recirculation zone near the vessel bottom, which may be a region where solids could possible accumulate because of the lower velocities associated with this region, especially in the vertical direction;

5. Simulations were conducted at different and increasing agitation speeds. Increasing the agitation speed resulted in an overall increase in the velocity distribution. However, some changes in the flow pattern were also noticed, especially in the region between impellers. This could be a real phenomenon or the result of a simulation artifact. Additional PIV data will be needed to confirm or not this finding;
6. The current results are important to industrial users of these vessels to understand the equipment that they use for industrial manufacturing (since detailed investigations of these systems are lacking), especially if the desired process outcome is not satisfactory;
7. Further studies are recommended to:
    a. Validate, through PIV, the CFD results in other regions of the vessels that were not investigated here;
    b. Determine the role of other variables, such as rheological properties of the fluid, on the hydrodynamics in the vessel
    c. Extend the investigation to other relevant mixing aspects, such as the determination of off-bottom solid suspension or mixing time.

REFERENCES

1. Dickey, D. S., Bittorf, K. J., Ramsey, C. J., Johnson, K. E. (2004). Understand Flow Patterns in Glass-lined Reactors. Chemical Engineering Progress, 100 (11), 21-25.

2. Anderson, J.D. (1995). Computational fluid dynamics: The basics with applications.1st Ed., pp. 1-212. New York, NY: McGraw-Hill.

3. Courant, R., Friedrichs, K., & Lewy, H. Die Partiellen Differenzengleichungen der Mathematischen Physik. Mathematische Annalen (English version: On the Partial Difference Equations of Mathematical Physics), 1928, 100, 32-74.

4. Parviz, M.; John, K. Tackling turbulence with supercomputers. Scientific American, 1997, 1, 276.

5. Wanot, J. Computational Fluid Dynamics Methods in Ship Design. R&D projects, 1996, Germany.

6. Sahu, A.K.; Kumar, P.; Patwardhan, A.W.; Joshi, J.B. CFD Modelling and Mixing in Stirred Tanks. Chemical Engineering Science 1999, 54 (13-14), 2285-2293.

7. Kieviet, F.G.; Van, R.J.; De Moor, P.P.E.A.; Kerkhof, P.J.A.M. Measurement and Modelling of the Air Flow Pattern in A Pilot-Plant Spray Dryer. Chemical Engineering Research and Design. 1997, 75 (A3), 321-328.

8. Kumar, A. Numerical Investigation of Secondary Flows in Helical Heat Exchangers. Institute of Food Technologists Annual Meeting. 1995, Anaheim, CA, USA. pp. 148.

9. Bakker, A.; Ahmad, H.H.; Lanre, M.O. Realize Greater Benefits from CFD. Fluid/Solids Handling. 2001, March, pp. 45-53.

10. Seader, J.D., & Henley, E.J. (1998). Separation process principles. 1st Ed., pp. 1-50. New York, NY: John Wiley & Sons, Inc.

11. Paul, E.L., Atiemo-Obeng, V.A., Kresta, S.M., & North American Mixing Forum. (2004). Handbook of industrial mixing: Science and practice. Hoboken, NJ: John Wiley & Sons, Inc.

12. Wilcox, D.C. (2004), Turbulence Modeling for CFD, 2nd Ed., DCW Industries, Inc.

13. Wilcox, D.C. (2008), Formulation of the k- ω Turbulence Model Revisited. AIAA Journal, Vol. 46, No. 11 (2008), pp. 2823-2838.

14. Batchelor, G. K. An Introduction to Fluid Dynamics. 1967, Cambridge University Press, Cambridge, England.